

**Effects of Latent Heat of Fusion on the Rapid  
Intensification of Hurricane Wilma (2005).**

---

William J. S. Miller

Advisor Da-Lin Zhang

Department of Atmospheric and Oceanic Science, University of Maryland  
College Park, Maryland

A scholarly paper in partial fulfillment of the requirements for the degree of

Master of Science

Submitted January 2015

## Abstract

The impacts of the latent heat of fusion on the rapid intensification (RI) of Hurricane Wilma (2005) are examined by comparing a 72-h control simulation (CTL) of the storm to a sensitivity simulation in which the latent heat of deposition is reduced by removing fusion heating (NFUS). Results show that while both storms undergo RI, the intensification rate is substantially reduced in NFUS. At peak intensity, NFUS is weaker than CTL by 30 hPa in minimum central pressure and by  $12 \text{ m s}^{-1}$  in maximum surface winds. The reduced rate of surface pressure falls in NFUS appears to result hydrostatically from less upper-level warming in the eye. It is shown that CTL generates more inner-core convective bursts (CBs) during RI, with higher altitudes of peak vertical motion in the eyewall, compared to NFUS. The latent heat of fusion contributes positively to sufficient eyewall conditional instability to support CB updrafts. Slantwise soundings taken in CB updraft cores reveal moist adiabatic lapse rates until 200 hPa, where the updraft intensity peaks. These results suggest that CBs may impact hurricane intensification by inducing compensating subsidence of the lower stratospheric air. We conclude that the development of more CBs inside the upper-level radius of maximum wind and the higher altitude of latent heating all appear to be favorable for RI of Wilma.

# Contents

List of Figures.....	iii
Chapter 1. Introduction.....	1
Chapter 2. Experiment Design.....	5
Chapter 3. Intensity Changes.....	7
Chapter 4. Convective Burst Statistics.....	16
Chapter 5. Vertical Motion Profiles.....	22
Chapter 6. Thermodynamic Characteristics of Convective Bursts.....	29
Chapter 7. Summary and Conclusions.....	36
Appendix I: Calculation of SCAPE.....	39
References.....	42

## List of Figures

- Figure 1. Time series of minimum central pressure ( $P_{\text{MIN}}$ ) and maximum 10-m windspeed ( $V_{\text{MAX}}$ ) for CTL (black) and NFUS (gray) from the 3-km resolution domain. Vertical lines denote characteristic times discussed in the text (solid for CTL and dashed for NFUS)..... 8
- Figure 2. Time series of temperature anomaly  $T'(z)$  (shaded, K, calculated with respect to 1000 km x 1000 km area-averaged  $\overline{T(z)}$  at initial time) and potential temperature (contours, K) at storm center for (a) CTL, and (b) NFUS from the 3-km resolution domain..... 10
- Figure 3. Radar reflectivity (shaded, dBz) and storm-relative flow vectors ( $\text{m s}^{-1}$ ) at  $z = 1$  km level with CB elements (orange crosses) and azimuthally-dependent  $z = 1$ -km RMW (blue dots) and  $z = 11$ -km RMW (black dots). Left panel shows CTL for (a) 15:00, (b) 20:00, (c) 32:30, and (d) 39:00. Right panel shows NFUS for (e) 19:00, (f) 24:00, (g) 39:00, and (h) 45:00. For (a),(b),(e), and (f), an 80 x 80 km subdomain is used (scale ticks mark 10-km intervals) while for (c),(d),(g), and (h), a 160 km x 160 km subdomain is used (scale ticks mark 20-km intervals). Upper right label boxes display total number of CB elements in the subdomain. Data for Fig. 3 and all subsequent figures are taken from the 1-km resolution domain..... 11
- Figure 4. Azimuthally averaged structures for (a, c) CTL at 32:30 and (b, d) NFUS at 39:00. Top row:  $T'(z)$  (shaded, K) with tangential winds (blue contours,  $\text{m s}^{-1}$ ), radial outflows (black contours, every 5  $\text{m s}^{-1}$ ), and upper-level radial

inflows (green contours, every  $0.5 \text{ m s}^{-1}$ ). Bottom row: total frozen hydrometeors (shaded,  $\text{g kg}^{-1}$ ) with vertical motion (upward, gray contours, 1, 3, 6, 9,  $12 \text{ m s}^{-1}$ ; downward, purple contours, -0.25, -0.5,  $-1 \text{ m s}^{-1}$ ) and with the freezing level marked in light blue. For in-plane flow vectors ( $\text{m s}^{-1}$ ) in (a)-(d) vertical motions are multiplied by three. Green dashed lines in (c,d) show radial boundaries of the slanted eyewall defined in section 5 at those times..... 13

Figure 5. Time series showing number of CB elements counted within the  $z = 11\text{-km}$  mean RMW (orange triangles) with average radius of CB occurrence (green crosses) for (a) CTL, and (b) NFUS. Mean  $z = 1\text{-km}$  and  $z = 11\text{-km}$  RMWs are shown as blue and black dots, respectively. Dashed vertical lines mark the beginning and end of the RI period..... 17

Figure 6. Histogram of the average number of updraft columns inside the  $z = 11\text{-km}$  mean RMW with  $w \geq 15 \text{ m s}^{-1}$  for (a) CTL, and (b) NFUS, binned by altitude of maximum vertical motion..... 19

Figure 7. Azimuthally-averaged SCAPE (shaded,  $\text{J kg}^{-1}$ ) with  $\theta_e$  at parcel lifting level (green dashed contours, K), eyewall boundaries (black solid contours, enclosing areas of  $w > 0.5 \text{ m s}^{-1}$  at lifting level), and mean  $z = 1\text{-km}$  RMW (blue dots) for (a) CTL, and (b) NFUS..... 21

Figure 8. Left panels: CCFAD of vertical motion for the eyewall, showing the percentage of gridpoints in the horizontal plane with vertical motion magnitudes greater than the abscissa-marked scale. Updrafts are shaded in orange for CTL and contoured in black for NFUS. Downdrafts are shaded in

blue for CTL and contoured in green for NFUS, following the same percentage intervals but with only the outer three lines labeled. Right panels: eyewall area-averaged upward ( $w > 0 \text{ m s}^{-1}$ , red) and downward ( $w < 0 \text{ m s}^{-1}$ , blue) vertical motion profiles with areal fraction of updraft core elements ( $w \geq 1 \text{ m s}^{-1}$ , black) and downdraft core elements ( $w \leq -1 \text{ m s}^{-1}$ , gray); CTL/solid, NFUS/dotted. Top row shows 20:00 CTL/24:00 NFUS, and bottom row shows 32:30 CTL/39:00 NFUS..... 23

Figure 9. As in Fig. 8 but for the outer rainband region..... 27

Figure 10. Total frozen hydrometeors integrated from 6-16 km (shaded,  $10^2 \text{ kg kg}^{-1}$ ) with horizontal storm-relative flow vectors ( $\text{m s}^{-1}$ ), vertical motion (upward, black contours, every  $5 \text{ m s}^{-1}$ ; downward, purple contours, -7, -5, -3, -1  $\text{m s}^{-1}$ ) and CB elements (white crosses) taken from (a) 20:00 CTL at  $z = 13 \text{ km}$ , and (b) 24:00 NFUS at  $z = 11 \text{ km}$ . Local  $z = 1\text{-km}$  and  $z = 11\text{-km}$  RMW are marked by black dots and gray circles, respectively. Dashed lines mark slice boundaries for azimuthal averaging in radial-height sections (c) and (d), which show radar reflectivity (shaded, dBz),  $\theta_e$  (black contours, K), vertical motion (upward, white contours, every  $5 \text{ m s}^{-1}$ ; downward, dotted gray contours, -4, -3, -2, -1, -0.5  $\text{m s}^{-1}$ ), and AAM (magenta contour,  $5 \times 10^5 \text{ s}^{-1}$ , 1.4 for CTL, 2.0 for NFUS), with in-plane flow vectors (vertical motions multiplied by 2). Slanted and vertical sounding lines are labeled with “S” and “V,” respectively. Black dots in (c) and (d) mark parcel lifting points used for SCAPE calculations..... 30

Figure 11. Left panels: skew  $T$ -log  $p$  diagrams for (a) CTL and (c) NFUS, with environmental variables taken from slanted sounding lines ( $S$ ), and with SCAPE computed along constant AAM lines, both from Fig. 10. Right panels: profiles along the slanted sounding lines of vertical motion ( $\text{m s}^{-1}$ ),  $\theta_e$  (K), and cloud species mixing ratios ( $\text{kg kg}^{-1}$ ; ( $\times 10^5$ ) for cloud ice, ( $\times 10^3$ ) for snow, graupel, cloud water, and rain) for (b) CTL and (d) NFUS. Dotted gray line marks the approximate freezing level height. For (a)-(d) top of plot marks 50 hPa level..... 32

Figure 12. As in Fig. 11 but for vertical sounding lines ( $V$ ) from Fig. 10..... 35

## Chapter 1. Introduction

There has been considerable interest during recent years in the understanding and prediction of rapid intensification (RI) of tropical cyclones (TCs), which is defined as a  $42 \text{ hPa day}^{-1}$  drop in minimum central pressure ( $P_{\text{MIN}}$ ) for western Pacific TCs (Holliday and Thompson 1979) or a  $15 \text{ m s}^{-1} \text{ day}^{-1}$  maximum surface wind speed ( $V_{\text{MAX}}$ ) increase for Atlantic TCs (Kaplan and DeMaria 2003). Hurricanes Opal (1995), Bret (1999), and Charley (2004) are examples of TCs that underwent unexpected RI episodes within 48 hours of making landfall on the U.S. coastline (Lawrence et al. 1998, 2001; Franklin et al. 2006), highlighting the need for improving our understanding of the RI process. Using the Statistical Hurricane Intensity Prediction Scheme (SHIPS) database, Kaplan and DeMaria (2003) identified environmental conditions being favorable for RI, which include warm sea surface temperatures (SSTs), weak vertical wind shear, stronger easterly winds in the upper troposphere, and high relative humidity in the lower troposphere. Clearly, these environmental conditions are not distinguished from those favoring tropical cyclogenesis and normal TC intensification rates. In addition, we have limited knowledge on the roles of inner-core processes, and on any potentially synergistic relationship between inner-core processes and favorable environmental conditions.

Observations have shown deep convective elements with anomalously cold cloud tops erupting near the center of TCs just prior to, or during RI (Rodgers et al. 1998, 2000; Price et al. 2009; Guimond et al. 2010; Fierro and Reisner 2011). We will adopt the most commonly used term, convective bursts (CBs), for this study. In their observational study of Hurricane Dennis (2005), Guimond et al. (2010) found  $20 \text{ m s}^{-1}$  eyewall updrafts at an altitude of 12-14 km, flanked by intense upper-level downdrafts of  $10\text{-}12 \text{ m s}^{-1}$ , several

hours before the storm commenced a period of RI. Heymsfield et al. (2001) showed CBs overshooting the tropopause by 2 km adjacent to the developing eye of Hurricane Bonnie (1998), and later, shortly before the storm reached maximum intensity, they found a deep mesoscale subsidence extending from  $z = 15$  km at cloud top downward and radially inward along the eye-eyewall interface. They hypothesized that this downdraft, originating as compensating subsidence of stratospheric air and being maintained by evaporative and sublimative cooling of hydrometeors detrained from the eyewall, may have contributed up to  $3^{\circ}\text{C}$  of warming aloft in the eye.

Hurricane Wilma (2005) underwent an 18-h RI period with a record-breaking deepening rate of  $83 \text{ hPa} (12 \text{ h})^{-1}$ , which culminated in the storm becoming the strongest hurricane ever recorded in the Atlantic basin, featuring a minimum central pressure of 882 hPa and maximum surface winds exceeding  $80 \text{ m s}^{-1}$ . In Part I of this series of papers (Chen et al. 2011, hereafter CZ11), the intensity and structural changes of Hurricane Wilma prior to, during, and after RI have been successfully reproduced with a 72-h (0000 UTC 18 October - 0000 UTC 21 October 2005) prediction using the Weather Research and Forecasting (WRF) model. Then, Zhang and Chen (2012, hereafter ZC12) used the hydrostatic equation to demonstrate how Wilma's developing upper level warm core, located at the same level as the outflow layer, is responsible for the largest portion of the surface pressure falls during RI. In Part II (Chen and Zhang 2013, hereafter CZ13), the collective action of a series of CBs straddling the radius of maximum wind (RMW) was shown to contribute to the warm core development through the cyclonic propagation of subsidence-induced warm anomalies into the region aloft in the eye. This result was consistent with the work of Hack and Schubert (1986), who showed that latent heat

release (LHR) inside the RMW, where inertial stability is large, is more efficient for TC intensification than that in the outer regions. CZ13 also found that reducing SSTs by 1°C everywhere in the domain significantly reduces the number of CBs and generates a considerably weaker warm core. This to certain extent conforms to the Wind-Induced Surface Heat Exchange (WISHE) hypothesis (Rotunno and Emanuel 1987; Emanuel et al. 1994), which describes TC intensification as primarily an air-sea interaction instability, although the characteristic slantwise neutral ascent cannot explain the generation of CBs of 10 – 20 m s<sup>-1</sup> in the eyewall.

Because of the important roles that CBs and the associated upper-level warming in the eye play in the RI of TCs, we are motivated to examine the impact of upper-level LHR associated with ice microphysical processes on the generation of CBs. For this study, we hypothesize that *LHR from deposition (vapor to ice) processes in the upper portion of the eyewall helps account for the development of CBs and that its occurrence within the RMW is the key to the RI of TCs*. Although there is ample evidence showing the reinvigoration of tropical oceanic updrafts at higher levels associated with ice LHR process (Zipser 2003; Romps and Kuang 2010; Fierro et al. 2009, 2012), few quantitative studies have been performed to examine how upper-level LHR inside the RMW is related to TC intensification. The effects of ice LHR processes on the RI of TCs have also been speculated (Guimond et al. 2010; Molinari and Vollaro 2010).

Thus, the objectives of this study are to (i) investigate the impact of upper-level depositional LHR on changes to TC structure and intensity through the generation of eyewall CBs; and (ii) examine the thermodynamic and ice microphysical structures of CBs in the eyewall. The above objectives will be achieved by comparing the Hurricane

Wilma prediction described in CZ11, ZC12 and CZ13, referred to hereafter as CTL, to a sensitivity simulation (NFUS) in which the latent heat of deposition is reduced, while all the other model parameters are kept identical, and then studying differences in intensity and structures. Through this study, we wish to answer the following questions: To what extent does the LHR from deposition determine the intensity and coverage of CBs, and what impact does this have on the RI of Hurricane Wilma? How will it affect the amplitude and altitude of the upper-level warm core? How will the vertical motion in the eyewall and rainband regions respond to the LHR from deposition?

The next chapter describes the WRF microphysics scheme and experimental design used to perform the NFUS experiment. Chapter 3 compares Wilma's intensity and structural changes between the CTL and NFUS simulations. Chapter 4 discusses CB statistics, and Chapter 5 analyzes the eyewall and rainband vertical motion profiles. Chapter 6 examines the thermodynamic and ice microphysical structures of CBs in the eyewall. A summary and concluding remarks are given in the final chapter.

## Chapter 2. Experiment Design

The 72-h CTL prediction uses the nonhydrostatic Advanced Research core of the WRF model (ARW, Version 3.1.1), with a quadruply-nested (27/9/3/1 km) grid and the initial and lateral boundary conditions that are identical to the Geophysical Fluid Dynamics Laboratory's then-operational data. Given the small changes in SST observed along Wilma's track during its RI period, time-independent SST fields, interpolated from the National Oceanic and Atmospheric Administration's (NOAA) Advanced Very High Resolution Radiometer (AVHRR) 0000 UTC 18 October SST data at 0.25 degree resolution, are used. All four domains use a vertical resolution of 55  $\sigma$  levels. See CZ11 for a detailed description of the model initialization and other physics options used. They include the Thompson et al. (2004, 2008) cloud microphysics scheme, which contains six classes of water substance (i.e., water vapor, cloud water, rain, snow, graupel, and cloud ice). In the Thompson scheme, depositional heating results from the deposition of vapor onto cloud ice, snow, and graupel, as well as from ice nucleation, while freezing heating is associated with liquid-to-ice processes, which include the homogeneous and heterogeneous freezing of water droplets, as well as the riming of graupel and snow. Our rationale for focusing on depositional heating impacts is based on the high altitude of this heat source and on the magnitude of the LHR. A parcel-following modeling study using the Lin-Farley-Orville microphysics scheme showed LHR from deposition to peak several kilometers higher than freezing heating in tropical oceanic cumulonimbus, perhaps as a result of more efficient warm-rain processes and lower CCN concentrations (relative to continental storms) causing rapid depletion of cloud water above the freezing level and limiting freezing heating to a shallow layer (Fierro et al. 2012). These results

were consistent with observations of radar reflectivity and cloud water concentrations decreasing more rapidly with height for TCs in comparison to land-based storms (Jorgensen et al. 1985, hereafter JZL). The strong dependence of CB activity on warm SSTs (CZ13) suggests that a high- $\theta_e$  (equivalent potential temperature) maritime boundary layer (MBL) environment could be a critical precondition for initiating updrafts strong enough to tap into depositional heating sources aloft. A significant buoyant acceleration boost should result from the much greater magnitude of the *latent heat of deposition* ( $L_d$ , 2838 J g<sup>-1</sup>) compared to the *latent heat of fusion* ( $L_f$ , 289 J g<sup>-1</sup>, see Rogers and Yau 1989); the difference between the two is the latent heat of vaporization ( $L_v$ ):  $L_d = L_v + L_f$ . To study the impacts of depositional LHR, the NFUS sensitivity simulation uses a modified microphysics scheme whereby the fusion component of depositional heating is removed so that  $L_d = L_v$ . No other aspects of the microphysics code are altered.

### Chapter 3. Intensity Changes

Figure 1 compares the time series of minimum central pressure ( $P_{\text{MIN}}$ ) and maximum surface (at  $z = 10$  m) wind speed ( $V_{\text{MAX}}$ ) between CTL and NFUS. Following an initial 15-h spin-up, CTL commences a period of rapid deepening in  $P_{\text{MIN}}$  and strengthening in  $V_{\text{MAX}}$ . By 32 h into the integration, hereafter 32:00,  $V_{\text{MAX}}$  levels off near  $72 \text{ m s}^{-1}$ , while  $P_{\text{MIN}}$  continues to fall, albeit less rapidly, until it reaches a minimum of  $890^1$  hPa around 36:00. Although seemingly inconsistent with the conventional pressure-wind relationship, the slower rate of  $V_{\text{MAX}}$  increase during the latter part of the rapid deepening phase has been attributed to intense frictional effects in Wilma's exceptionally small eyewall and to the lack of any further contraction (CZ11; Kieu et al. 2010). This 21-h (i.e., 15:00–36:00) period is characterized by a  $P_{\text{MIN}}$  drop of 78 hPa and a  $V_{\text{MAX}}$  increase of  $27 \text{ m s}^{-1}$ , easily exceeding the conventional RI threshold, and we will refer to it as the CTL RI phase for the remainder of this study. After 36:00, a developing outer eyewall begins cutting off the supply of high- $\theta_e$  air to the inner core region, weakening the storm and beginning an eyewall replacement cycle (ERC). Beyond 54:00, as the outer eyewall begins to contract,  $P_{\text{MIN}}$  reaches a steady state while  $V_{\text{MAX}}$  gradually increases.

Removal of the fusion component of depositional heating results in a significantly weaker storm at the time of peak intensity, with a 30 hPa increase in  $P_{\text{MIN}}$  (920 hPa in NFUS versus 890 hPa in CTL) and a  $12 \text{ m s}^{-1}$  drop in  $V_{\text{MAX}}$  ( $60 \text{ m s}^{-1}$  in NFUS versus  $72 \text{ m s}^{-1}$  in CTL). At 19:00, a sustained period of rapid  $P_{\text{MIN}}$  falls begins, lasting

---

<sup>1</sup> Slight differences in peak intensity and intensification rate from those reported in CZ11 (890 hPa vs. 889 hPa and  $6 \text{ hPa h}^{-1}$  vs.  $7 \text{ hPa h}^{-1}$ ), as well as small differences in other fields, likely result from use of different WRF data postprocessing packages.

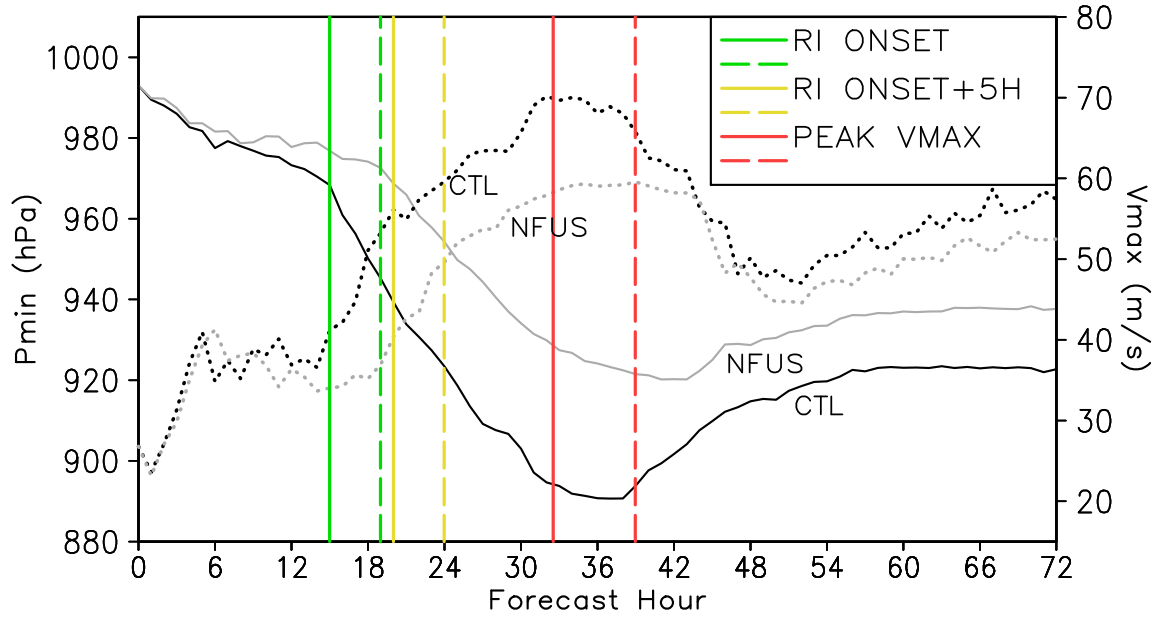


Figure 1. Time series of minimum central pressure ( $P_{\text{MIN}}$ ) and maximum 10-m windspeed ( $V_{\text{MAX}}$ ) for CTL (black) and NFUS (gray) from the 3-km resolution domain. Vertical lines denote characteristic times discussed in the text (solid for CTL and dashed for NFUS).

through 35:00, at which time  $P_{\text{MIN}}$  begins falling at a rate of  $0.9 \text{ hPa h}^{-1}$  until it reaches a minimum at 42:00. Despite showing a reduced intensification rate, the NFUS 19:00-35:00 period still qualifies as RI per the conventional definition, with an average deepening rate of  $3.0 \text{ hPa h}^{-1}$ . After reaching peak intensity, NFUS also undergoes an ERC and weakens before gradually reintensifying with the contraction of the new eyewall. The intensity differences become less pronounced following the ERC, and the simulation ends with NFUS 15 hPa weaker than CTL. Comparing the model-predicted tracks for the two simulations (not shown), the differences never exceed 0.5 degrees latitude or longitude and both storm tracks remain over the same SST environment, leading the authors to conclude that the intensity differences presented in Fig. 1 are not caused by environmental influences.

In summary, the NFUS storm undergoes the same basic structural changes observed in CTL. While NFUS still undergoes RI, the onset is 4 h later, the duration is 5 h shorter, and the average deepening rate over the RI period is lower (namely,  $3.0 \text{ hPa h}^{-1}$  for 19:00-35:00 versus  $3.7 \text{ hPa h}^{-1}$  for 15:00-36:00 in CTL). The peak hourly deepening rate is slightly reduced ( $5 \text{ hPa h}^{-1}$  versus  $6 \text{ hPa h}^{-1}$  in CTL). The remainder of this study will focus primarily on the RI period.

To see how the RI in  $P_{\text{MIN}}$  differs between the two simulations, Fig. 2 compares their time-height cross sections of perturbation temperatures  $T'(z, t)$ , along with potential temperature  $\theta$ , taken at the eye center. For both simulations, the  $\theta = 370 \text{ K}$  surface begins to descend at RI onset (15:00 CTL/19:00 NFUS), commencing a period of increased upper-level warming. Between 33:00 and 58:00, NFUS develops a  $12\text{-}14^\circ\text{C}$  warm anomaly, which is still significant but far less substantial than the peak warming of over  $20^\circ\text{C}$  that CTL shows at 36:00. As discussed in CZ13, this upper-level warming should primarily result from the subsidence of stratospheric air. During the course of RI, the NFUS isentropic surfaces fail to descend as far, with the  $\theta = 370 \text{ K}$  contour lowering to  $z = 9 \text{ km}$  and  $z = 11 \text{ km}$  in CTL and NFUS, respectively, and with the  $\theta = 390 \text{ K}$  contour never dipping below  $z = 16 \text{ km}$  in NFUS, despite the fact that it reaches  $z = 14 \text{ km}$  at 36:00 in CTL. Throughout the RI period, the warm core remains in the upper troposphere, near  $z = 14 \text{ km}$  in CTL and roughly  $1 \text{ km}$  lower in NFUS. It appears likely, based on the hydrostatic arguments of ZC12, that the weaker NFUS upper-level warming accounts for a large portion of the 30-hPa reduction in peak storm intensity.

Since CZ13 attributed the CTL-simulated intense upper-level warm core to the development of CBs, Fig. 3 compares the distribution of CB elements relative to the

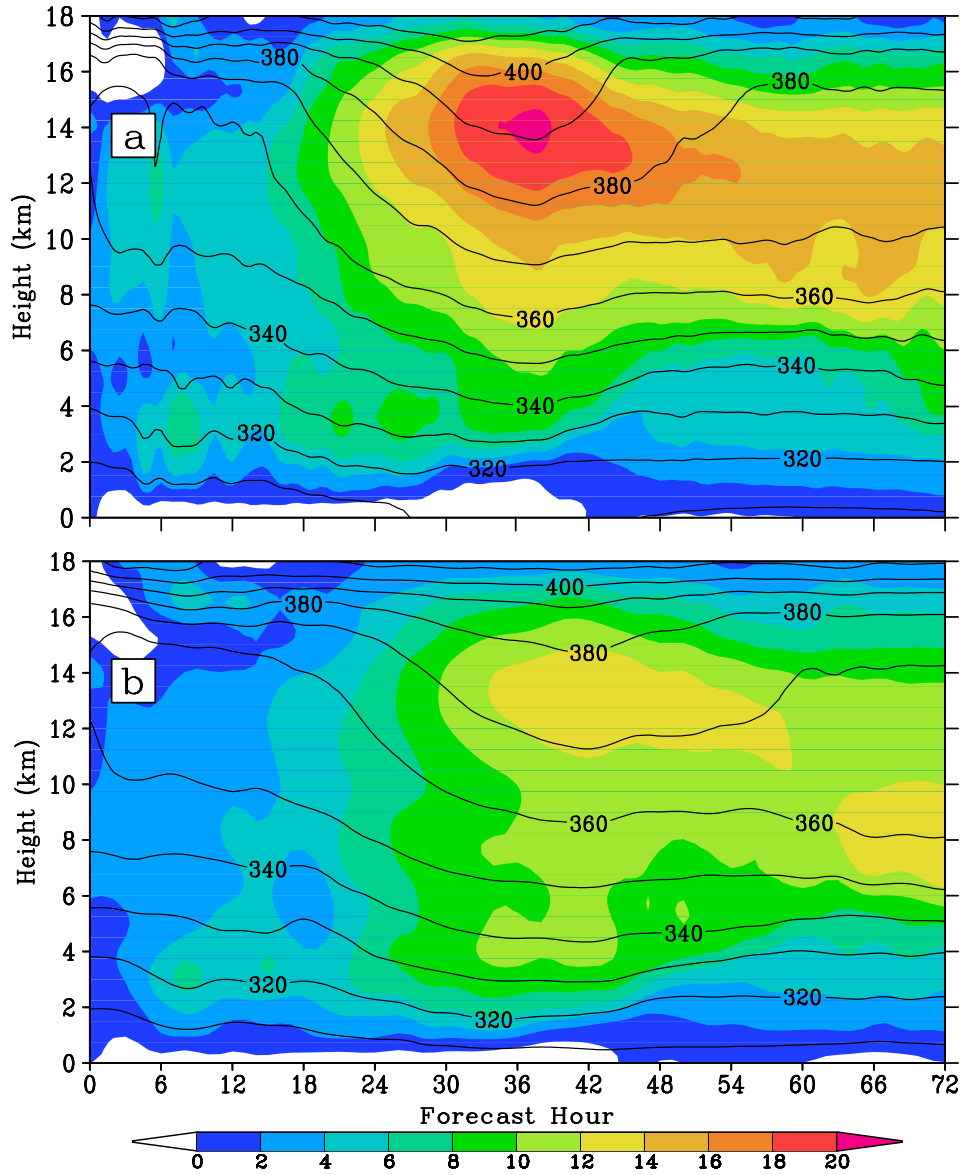


Figure 2. Time series of temperature anomaly  $T'(z)$  (shaded, K, calculated with respect to 1000 km x 1000 km area-averaged  $\overline{T(z)}$  at initial time) and potential temperature (contours, K) at storm center for (a) CTL, and (b) NFUS from the 3-km resolution domain.

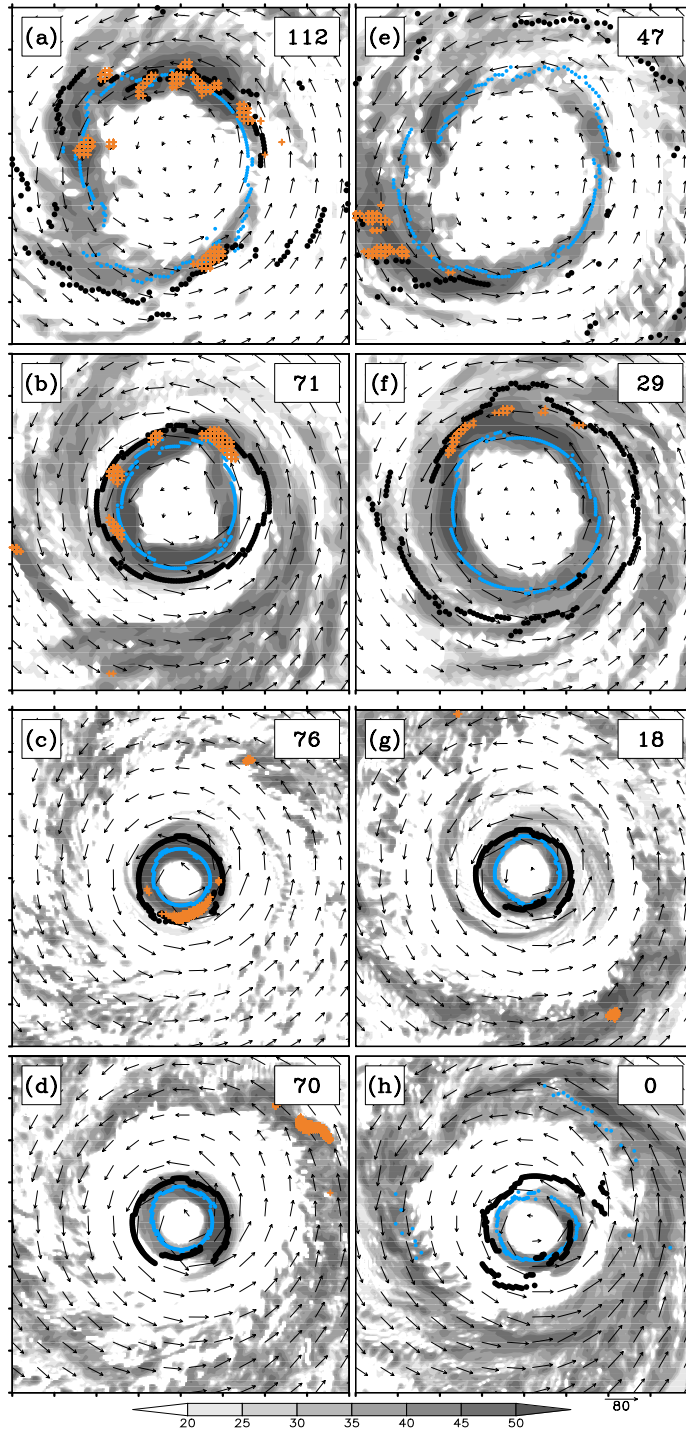


Figure 3. Radar reflectivity (shaded, dBz) and storm-relative flow vectors ( $\text{m s}^{-1}$ ) at  $z = 1$  km level with CB elements (orange crosses) and azimuthally-dependent  $z = 1$ -km RMW (blue dots) and  $z = 11$ -km RMW (black dots). Left panel shows CTL for (a) 15:00, (b) 20:00, (c) 32:30, and (d) 39:00. Right panel shows NFUS for (e) 19:00, (f) 24:00, (g) 39:00, and (h) 45:00. For (a),(b),(e), and (f), an  $80 \times 80$  km subdomain is used (scale ticks mark 10-km intervals) while for (c),(d),(g), and (h), a  $160 \text{ km} \times 160 \text{ km}$  subdomain is used (scale ticks mark 20-km intervals). Upper right label boxes display total number of CB elements in the subdomain. Data for Fig. 3 and all subsequent figures are taken from the 1-km resolution domain.

RMW, together with radar reflectivity at  $z = 1$  km and  $z = 11$  km, taken at a few timesteps. The CB elements are counted<sup>2</sup> by the same procedure as that used by CZ13, i.e., vertical grid columns identified that contain at least one point with  $w \geq 15$  m s<sup>-1</sup> at or above  $z = 11$  km. For both simulations, the RI period is characterized by a contracting and increasingly coherent eyewall, evident in both the radar reflectivity trends and in the tendency for the local  $z = 1$ -km and  $z = 11$ -km RMWs to follow an increasingly circular pattern about the storm center (Figs. 3a-c for CTL, and Figs. 3e-g for NFUS). During this period, CB activity remains concentrated near and inside the  $z = 11$ -km RMW, where the inertial stability and the efficiency of LHR for TC intensification are high (Hack and Schubert 1986). This is especially apparent once the upper-level tangential wind fields have become more symmetric in CTL (Fig. 3b) and in NFUS (Fig. 3f). By 39:00 CTL/45:00 NFUS, both storms are in the midst of an ERC (Figs. 3d,h), as shown by the collapse of inner eyewall convection with the development of an outer eyewall near the 60 km radius. For CTL, CB elements now cluster in the outer eyewall, whereas previously they had remained near the  $z = 1$ -km RMW, where  $\theta_e$  and convergence had been maximized in the MBL. The following section will present a more detailed analysis of CB activity and its impact on the RI of both storms.

Figure 4 compares azimuthally averaged structures at the time of peak  $V_{\text{MAX}}$  (32:30 CTL/39:00 NFUS, Fig. 1). Before discussing the differences, it should be noted that both CTL and NFUS display the classic “in-up-out” secondary circulation of a mature TC, with a low-level inflow peaking just outside the RMW, a titled updraft core, and an

---

<sup>2</sup> Note that CZ13 counted CB elements from 3 time levels at 5 min intervals, whereas they are counted herein only from one time level, thus causing less CB elements to be seen at  $t = 15:00$  (cf. Fig. 3a herein and Fig. 3d in CZ13).

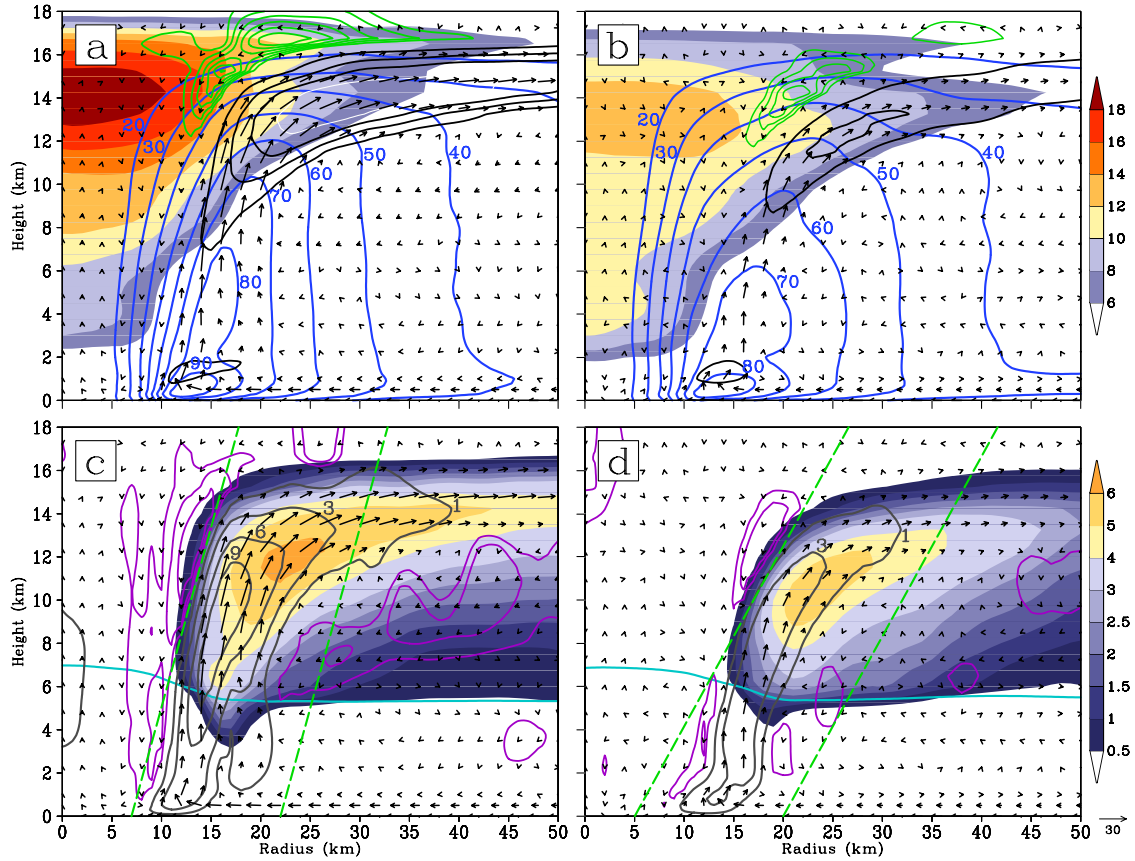


Figure 4. Azimuthally averaged structures for (a, c) CTL at 32:30 and (b, d) NFUS at 39:00. Top row:  $T'(z)$  (shaded, K) with tangential winds (blue contours,  $\text{m s}^{-1}$ ), radial outflows (black contours, every  $5 \text{ m s}^{-1}$ ), and upper-level radial inflows (green contours, every  $0.5 \text{ m s}^{-1}$ ). Bottom row: total frozen hydrometeors (shaded,  $\text{g kg}^{-1}$ ) with vertical motion (upward, gray contours, 1, 3, 6, 9, 12  $\text{m s}^{-1}$ ; downward, purple contours,  $-0.25, -0.5, -1 \text{ m s}^{-1}$ ) and with the freezing level marked in light blue. For in-plane flow vectors ( $\text{m s}^{-1}$ ) in (a)-(d) vertical motions are multiplied by three. Green dashed lines in (c,d) show radial boundaries of the slanted eyewall defined in section 5 at those times.

upper-level main outflow branch in the  $z = 10$  to  $z = 16$  km layer (Figs. 4a,b). Like CTL, NFUS shows two features identified in ZC12 and CZ13 that facilitate upper-level warm core development. First, the upper-level outflow layer coincides with the height of the warm core, helping protect the warmer air inside the RMW from ventilation by

environmental flows. Additionally, both generate an upper-level return inflow branch that extends downward from above the main outflow into the eye region near the altitude of peak warming (Figs. 4a,b). Driven by the mass sink and upper-level convergence above the eye and maintained by evaporative/sublimative cooling from detrained eyewall hydrometeors, the return inflow may contribute to warm core development by drawing down stratospheric air (ZC12).

Despite these similarities, CTL shows a deeper and more intense primary circulation. Comparing the tangential wind fields, CTL and NFUS peak above 90 and 80  $\text{m s}^{-1}$ , respectively, around  $z = 1 \text{ km}$ , with  $70 \text{ m s}^{-1}$  winds extending as high as  $z = 10 \text{ km}$  in CTL but only to  $z = 6 \text{ km}$  in NFUS (Figs. 4a,b). For CTL, the peak low-level inflow is  $5 \text{ m s}^{-1}$  stronger ( $30 \text{ m s}^{-1}$  versus  $25 \text{ m s}^{-1}$ , not shown) with a deeper inflow depth, while the upper-level outflow branch is 2-4 times more intense (cf. Figs. 4a,b).

Figs. 4c,d compare the azimuthally averaged vertical motion with total frozen hydrometeors, defined here as the integrated cloud ice, snow and graupel mixing ratios. The CTL updraft core (Fig. 4c) is significantly stronger, with  $w$  exceeding  $9 \text{ m s}^{-1}$  between  $z = 6$  and  $z = 12 \text{ km}$ . NFUS, by comparison, shows peak updrafts of  $3\text{-}6 \text{ m s}^{-1}$  extending through the depth of the eyewall (Fig. 4d). For both CTL and NFUS, total frozen hydrometeors peak just outside the upper portion of the updraft core. This results from the fact that cloud ice initiates in the updraft region and then grows by deposition to snow while being advected outward by the main outflow (not shown). The peak frozen hydrometeor mixing ratio in CTL is  $1 \text{ g kg}^{-1}$  greater in magnitude, and located  $1 \text{ km}$  higher. Any difference in the cloud species fields must result from differences in the flow fields as a response to differences in LHR, since the microphysical mass transfer

processes in CTL and NFUS are kept identical. It certainly appears plausible that the stronger CTL updraft core, with peak updrafts more closely aligned with peak frozen hydrometeor mixing ratios, may result from enhanced buoyancy generated by the greater magnitude of  $L_d$ .

## Chapter 4. Convective Burst Statistics

CZ13 showed how CB-induced compensating subsidence could significantly contribute to the development of an upper-level warm core after an upper-level cyclonic circulation develops around the time of RI onset. Meanwhile, a reduction in static stability, resulting from the downward displacement of upper level isentropes, lowers the energy dispersion of internal gravity waves. Nevertheless, the modest CB-induced warming in the eye during the pre-RI stage allows for the development of the upper-level cyclonic flows as a result of local thermal wind balance. Based on these findings, and on the thermal efficiency arguments of Hack and Schubert (1986), we choose to focus herein on CB activity inside the azimuthally-averaged  $z = 11$ -km RMW.

The time series in Figure 5 shows the number of CB elements, counted inside the  $z = 11$ -km RMW, along with the mean CB radius and the  $z = 1$ -km and  $z = 11$ -km RMWs. The CTL CB activity reaches a peak in the first few hours, attributed by CZ13 to high CAPE in the bogussed vortex at  $t = 0$  h, followed by a sharp decline until ON, after which it remains at a stable level throughout the rest of the RI period (Fig. 5a). After the RI period ends at 36:00, inner-core CB activity all but disappears, which is consistent with observational findings of other storms (Molinari et al. 1999). Note that the large cluster of 70 CB elements at 39:00, shown in Fig. 3d, is not counted here because the mean  $z = 11$ -km RMW has not yet jumped to the outer eyewall. The NFUS simulation (Fig. 5b) shows a similar overall trend, but with significantly reduced CB activity throughout the pre-RI and RI periods. It follows that by removing the fusion component

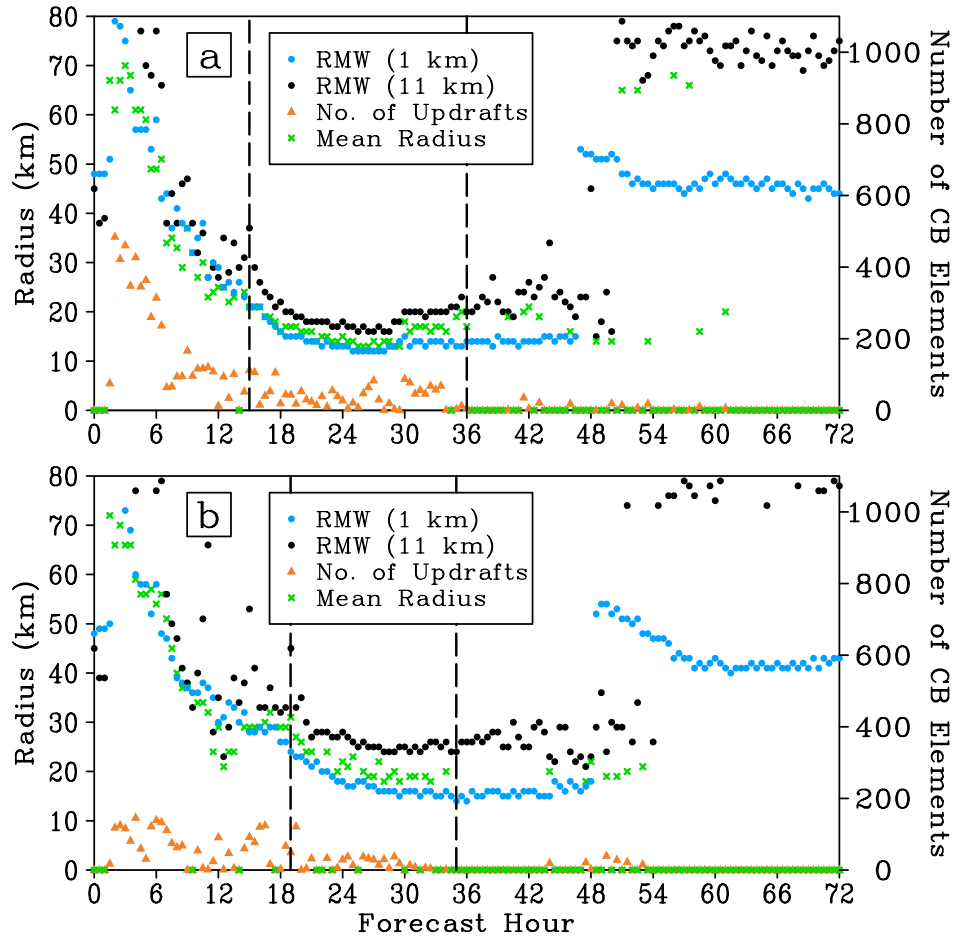


Figure 5. Time series showing number of CB elements counted within the  $z = 11$ -km mean RMW (orange triangles) with average radius of CB occurrence (green crosses) for (a) CTL, and (b) NFUS. Mean  $z = 1$ -km and  $z = 11$ -km RMWs are shown as blue and black dots, respectively. Dashed vertical lines mark the beginning and end of the RI period.

of depositional heating, CB activity inside the  $z = 11$ -km RMW becomes less prevalent both prior to and during RI, coinciding with a weaker, more slowly developing upper-level warm core and a more modest rate of surface pressure falls.

Figure 6 compares histograms of maximum vertical motion altitude for updrafts peaking at or above  $15 \text{ m s}^{-1}$ , at any height, for the pre-RI, RI, and post-RI periods. During pre-RI, the majority of intense CTL updrafts peak in the upper troposphere, with

the largest number peaking at  $z = 14$  km. Then, during RI, the favored peak updraft height lowers to 9 km with a secondary maximum appearing at 6 km near the freezing level, although a substantial number of updrafts still peak above  $z = 10$  km. During post-RI, the very small number of updrafts that reach  $15 \text{ m s}^{-1}$  peak near the freezing level. NFUS shows fewer  $w \geq 15 \text{ m s}^{-1}$  updrafts during the pre-RI and RI phases, with the differences most pronounced in the upper troposphere. For pre-RI, the strong sharp peak at 14 km is no longer present, replaced by a broader, weaker peak spanning the 9-14 km range. Note the greater than threefold reduction in number of occurrences at  $z = 14$  km relative to CTL. During RI, NFUS shows similar numbers of intense updrafts at the favored  $z = 6$  km and  $z = 9$  km levels, but for heights above  $z = 10$  km, the NFUS intense updraft count is reduced from CTL by at least one half. The lower frequency of intense NFUS updrafts peaking above  $z = 10$  km during the pre-RI and RI stages suggests that 1) depositional heating plays a crucial role in generating intense updrafts at these levels, and that 2) these updrafts may be important to the development of an upper-level warm core in a rapidly intensifying TC (cf. Figs. 2a,b). Although observational studies have shown that not all CBs induce subsidence flowing into the eye region (Heymsfield et al. 2001), we hypothesize that reduced NFUS CB activity during the RI period results in an overall weaker contribution of subsidence-induced warming toward warm-core development.

Since CB development requires the presence of sufficient conditional instability, Figure 7a plots Slantwise Convective Available Potential Energy (SCAPE, see Appendix I) in CTL over the RI period. Using this method, parcel buoyancy is calculated along slantwise trajectories following constant absolute angular momentum (AAM) surfaces, in

contrast to conventional CAPE, where parcel trajectories are vertical. Over the eye region, the steep slope of the AAM surfaces (not shown) makes SCAPE effectively equal

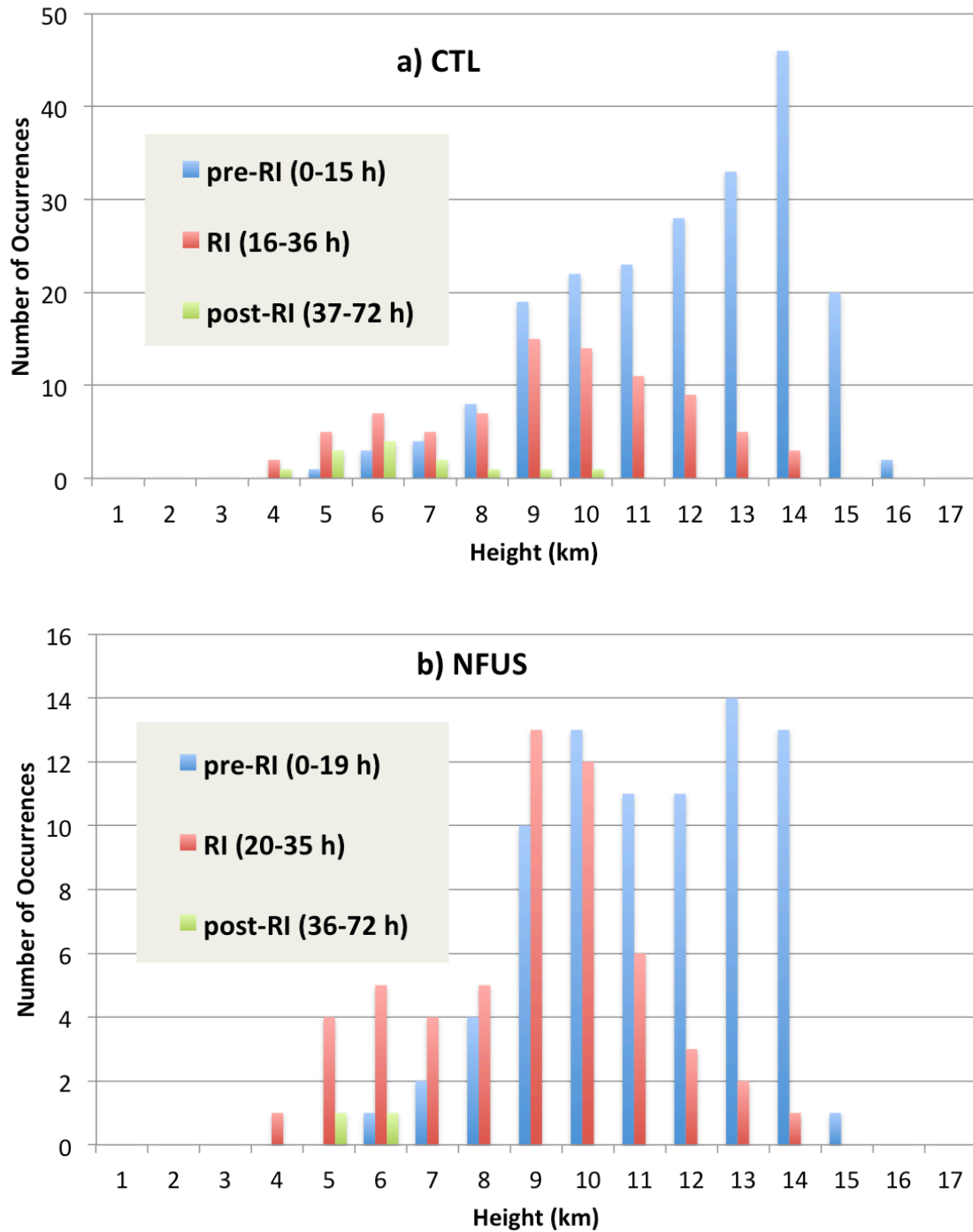


Figure 6. Histogram of the average number of updraft columns inside the  $z = 11$ -km mean RMW with  $w \geq 15 \text{ m s}^{-1}$  for (a) CTL, and (b) NFUS, binned by altitude of maximum vertical motion.

to CAPE, and we see a rapid reduction in SCAPE coincident with the marked upper-level warming following RI onset, a result similar to that shown for Super Typhoon (STY) Megi (Wang and Wang 2014). Although the eyewall shows negligible CAPE (not shown), eyewall SCAPE remains greater than  $400 \text{ J kg}^{-1}$  during RI, which is sufficient to sustain peak updrafts at the LNB ( $w_{\text{max}}$ ) of about  $30 \text{ m s}^{-1}$  (see Fig. 6 in CZ13) using the approximation

$$w_{\text{max}} = \sqrt{2 \text{ SCAPE}},$$

assuming an undiluted ascent in the updraft core. After 18 h, the reservoir of the highest SCAPE shifts from the inner edge to the outer edge of the eyewall, a result supporting the findings of Frisius and Schönemann (2012) that SCAPE outside a TC eyewall could cause superintensity.

The NFUS eyewall (Figure 7b) shows reduced SCAPE, although the  $200 \text{ J kg}^{-1}$  available throughout the RI period is still sufficient to generate  $20 \text{ m s}^{-1}$  updrafts. When calculating NFUS lifted parcel temperatures, ice heating is not permitted, whereas for CTL, the ice adiabat is followed above the freezing level. Despite the fact that the microphysical assumptions used in the SCAPE calculations lack the complexity of the Thompson microphysics scheme (and suppress NFUS freezing heating, which is allowed in the NFUS WRF code), they show that parcel warming from ice LHR is an important contributor to SCAPE in Wilma's eyewall, especially given the warmer environmental temperatures experienced by CTL parcels rising along constant AAM surfaces (not shown).

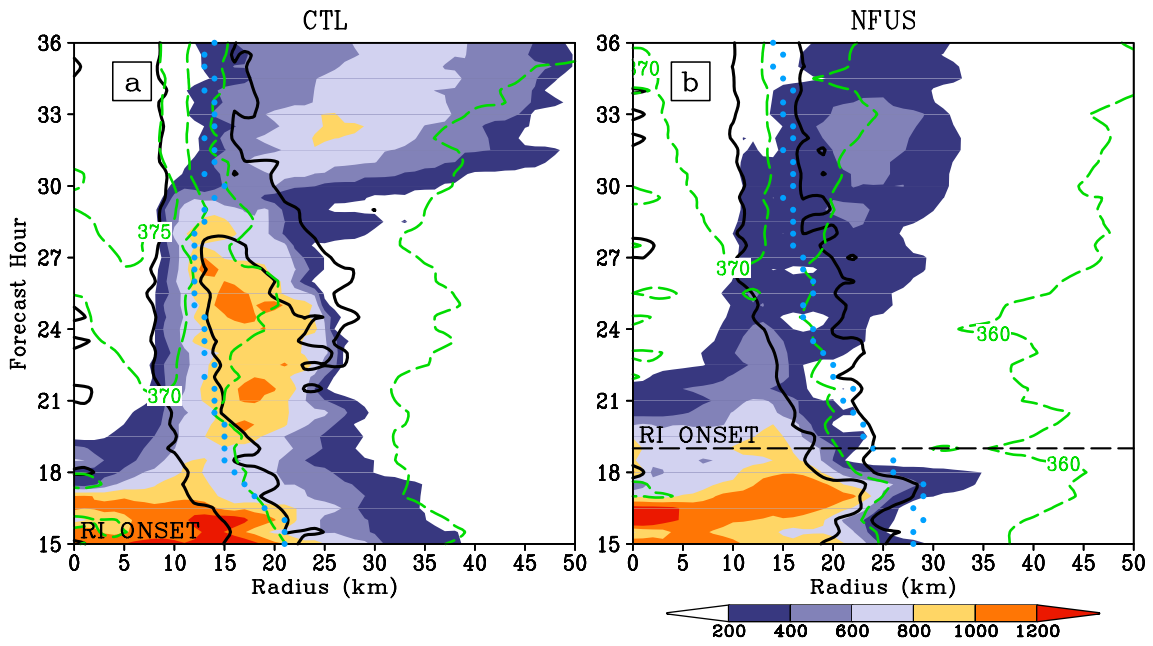


Figure 7. Azimuthally-averaged SCAPE (shaded,  $\text{J kg}^{-1}$ ) with  $\theta_e$  at parcel lifting level (green dashed contours, K), eyewall boundaries (black solid contours, enclosing areas of  $w > 0.5 \text{ m s}^{-1}$  at lifting level), and mean  $z = 1\text{-km}$  RMW (blue dots) for (a) CTL, and (b) NFUS.

## Chapter 5. Vertical Motion Profiles

We now compare the CTL and NFUS vertical motion profiles, with more focus on how depositional heating affects the full range of updraft intensities, for both the eyewall and the outer rainbands. This is done by utilizing Cumulative Contoured Frequency by Altitude Diagrams (CCFADs, Yuter and Houze 1995b), which show, for a given height, the percentage of horizontal gridpoints with vertical motion weaker than the abscissa scaled value. The inner and outer radial boundaries are assigned based on the azimuthally-averaged  $w$  field such that 1) the  $1 \text{ m s}^{-1}$  contour at  $z = 8 \text{ km}$  and 2) the  $3 \text{ m s}^{-1}$  contour at all heights are fully enclosed, keeping the CTL and NFUS widths the same for each comparison time. The “outer rainbands,” by our definition, include all points from 20 km outside the  $z = 11 \text{ km}$  RMW to the edge of a  $200 \text{ km} \times 200 \text{ km}$  box surrounding the storm center. All vertical motion data shown in Figs. 8-9 are composited from a  $\pm 1\text{-h}$  time window at 30-min intervals.

### *a. Eyewall*

Figure 8 shows CCFADs (left panels) and area-averaged vertical motion ( $\overline{w(z)}$ ) profiles (right panels) for the eyewall at two selected times. Five hours after RI onset (20:00 CTL/24:00 NFUS), CTL shows an increased broadening of the updraft distribution with height, with the 95<sup>th</sup> percentile peaking at  $14 \text{ m s}^{-1}$  near  $z = 10 \text{ km}$ , and with the 99.9<sup>th</sup> percentile peaking even higher, at  $27 \text{ m s}^{-1}$  near  $z = 13 \text{ km}$  (Fig. 8a). Although Black et al. (1996) found weaker eyewall updrafts in a composite sample of airborne Doppler radar vertical motion data taken from seven hurricanes, with the 95<sup>th</sup>

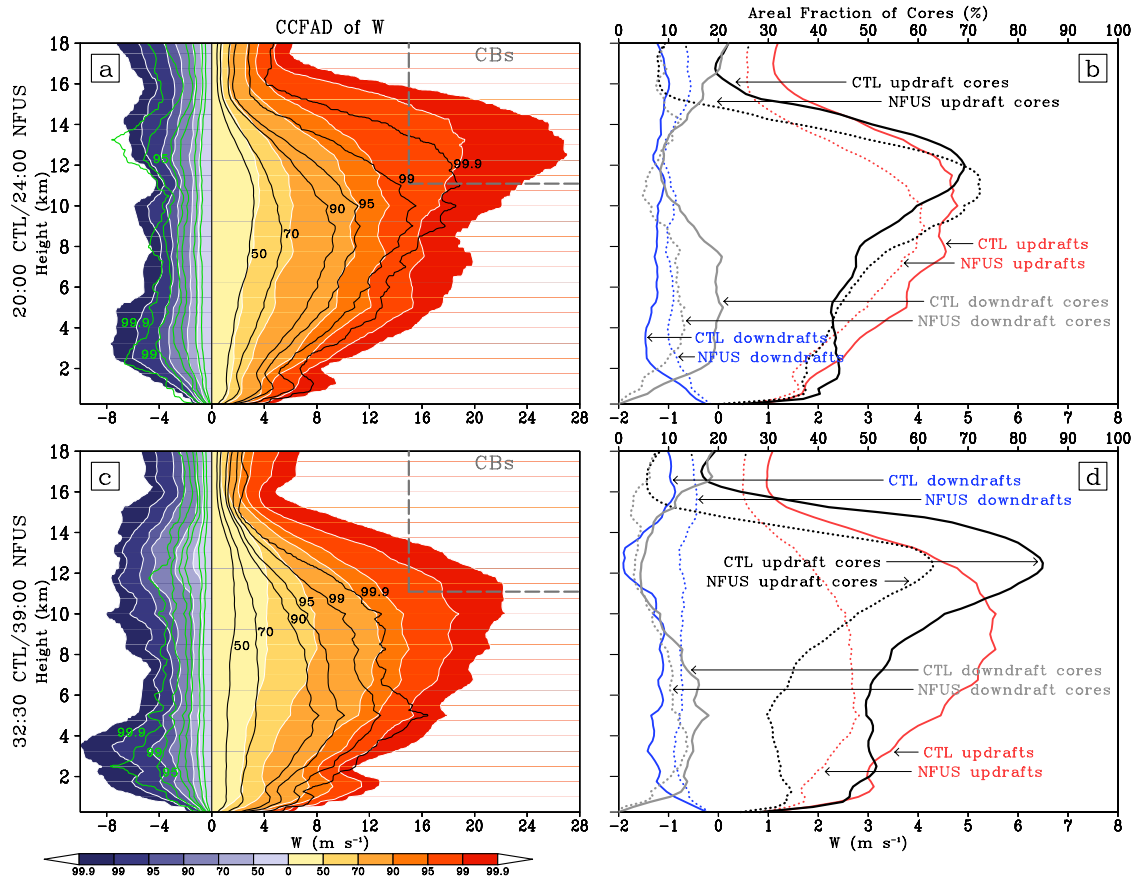


Figure 8. Left panels: CCFAD of vertical motion for the eyewall, showing the percentage of gridpoints in the horizontal plane with vertical motion magnitudes greater than the abscissa-marked scale. Updrafts are shaded in orange for CTL and contoured in black for NFUS. Downdrafts are shaded in blue for CTL and contoured in green for NFUS, following the same percentage intervals but with only the outer three lines labeled. Right panels: eyewall area-averaged upward ( $w > 0 \text{ m s}^{-1}$ , red) and downward ( $w < 0 \text{ m s}^{-1}$ , blue) vertical motion profiles with areal fraction of updraft core elements ( $w \geq 1 \text{ m s}^{-1}$ , black) and downdraft core elements ( $w \leq -1 \text{ m s}^{-1}$ , gray); CTL/solid, NFUS/dotted. Top row shows 20:00 CTL/24:00 NFUS, and bottom row shows 32:30 CTL/39:00 NFUS.

updraft percentile exceeding  $5 \text{ m s}^{-1}$  ( $6 \text{ m s}^{-1}$  in the upper troposphere), their eyewall updraft core (“Doppler draft”) average and maximum velocities peaked in the upper troposphere near  $z = 13 \text{ km}$ . Marks and Houze (1987), also using Doppler radar-derived

vertical velocities, found the strongest updrafts in Hurricane Alicia's eyewall on the order of 5-12  $\text{m s}^{-1}$  in the  $z = 6-14$  km range, with the highest values above  $z = 10$  km. However, given our focus on an RI storm and the possibility that the aircraft penetrations may have missed the most intense eyewall updrafts, either by chance or for safety reasons, direct comparison with these studies is rather difficult. Stronger vertical motion may be a characteristic of RI TCs, as the Hurricane Emily eyewall contained peak updrafts and downdrafts of 24 and 19  $\text{m s}^{-1}$ , respectively, with mean updrafts and downdrafts roughly two times the strength of those found in other TCs (Black et al. 1994).

The NFUS CCFAD (Fig. 8a) has a similar shape, but significant differences appear in the highest altitudes for the most intense updrafts: at  $z = 14$  km, for example, the strongest 1% of NFUS updrafts exceed 6  $\text{m s}^{-1}$  while the strongest 1% of CTL updrafts exceed 18  $\text{m s}^{-1}$ . Consistent with the moderate strength portion of the CCFAD distributions (70<sup>th</sup> percentiles and below), the  $\overline{w(z)}$  profiles (Fig. 8b) show smaller differences, but the discrepancies become wider in the  $z = 11-15$  km range. Figure 8b also compares the areal fraction of core elements, defined here as gridpoints with  $|w| \geq 1$   $\text{m s}^{-1}$ , following the convention of JZL but without imposing any spatial continuity requirements. Above  $z = 8$  km, the CTL updraft core fraction sharply increases to a maximum of 70% near  $z = 12$  km. Although the maximum NFUS updraft core fraction is slightly greater, it peaks 1 km lower, and above  $z = 14$  km it remains roughly 10% less than CTL. Together, the CCFAD,  $\overline{w(z)}$ , and core element fraction profiles provide further evidence of updraft enhancement by depositional LHR at the upper levels during

the early stages of RI, with the strongest impacts on the most intense 5% of updrafts above  $z = 10$  km.

At the time of the highest  $V_{\text{MAX}}$  (32:30 CTL/39:00 NFUS), the peak CTL updraft altitude shifts lower, to near  $z = 10$  km, as seen both in the CCFAD broadening (Fig. 8c) and in  $\overline{w(z)}$  (Fig. 8d). Wang and Wang (2014) showed a similar lowering of the peak updraft height during the course of the STY Megi RI, and they attributed increased eyewall tilt and stabilization from upper-level warming, both of which are seen for CTL (Figs. 2a and 5a), as possible causes. Nevertheless, intense updrafts satisfying the CB criterion remain embedded in the eyewall (cf. Figs. 3c, 5a, and 8c). The updraft maximum below  $z = 2$  km likely results from the enhanced Ekman pumping process in the eyewall (Liu et al. 1999; Zhang and Kieu 2006). The NFUS CCFAD (Fig. 8c) now shows greater differences. For the 90<sup>th</sup> updraft velocity percentile and above, the peak shifts considerably lower, to  $z = 5$  km; at higher altitudes the vertical motions are now weaker, relative to CTL, and CB elements are no longer present. This might result from 1) a more tilted eyewall (cf. Figs. 5a,b) and 2) reduced LHR available to generate parcel buoyancy in the warmer upper-level environment (Fig. 2b). In the middle levels, the moderate-strength NFUS updrafts in the CCFAD and  $\overline{w(z)}$  profile (Fig. 8d) are roughly 50% of their counterparts in CTL; these differences are consistent with the weaker azimuthally-averaged NFUS midlevel updraft core and larger areal coverage of CTL updrafts within the 15-km wide annulus used to calculate probabilities (Figs. 4c,d). The wider CTL updraft core at peak intensity should primarily result from the merging of a secondary eyewall after 27:00 (Fig. 12 in CZ11). The concomitant increase in eyewall upward mass flux might explain why CTL continues to rapidly intensify in the few hours

following this merger, even reaching its peak hourly intensification rate during this time (Fig. 1).

We now examine the eyewall downdrafts in Fig. 8, focusing on the upper levels. Upper-level subsidence flanking updraft cores has been documented in rapidly intensifying TC eyewalls (Black et al. 1994, Heymsfield et al. 2001, Guimond et. al 2010), and as shown by CZ13, it enhances upper-level warm core development when directed toward the eye. For NFUS 5 h into RI, note the reduced CCFAD broadening (Fig. 8a), smaller downdraft core fraction, and  $0.3 - 0.5 \text{ m s}^{-1}$  lower downdraft  $\overline{w(z)}$  (Fig. 8b) above  $z = 14 \text{ km}$ . Larger differences in upper-level subsidence are apparent at the time of peak  $V_{\text{MAX}}$  (Figs. 8c,d), and we can expect much of the stronger CTL upper-level subsidence to be directed toward the eye, given the well-developed return inflow above  $z = 15 \text{ km}$  in the CTL eyewall (Figs. 4a,c).

#### *b. Outer rainbands*

To see how the vertical motion profiles in the eyewall differ from those in the outer regions, we plot vertical motion profiles for the outer rainbands consisting of convective, stratiform and nonprecipitating regions. Fig. 9 shows that the outer rainbands are characterized by weaker updrafts and a smaller area covered by cores relative to the eyewall, confirming the earlier findings of JZL and Black et al. (1996). For both times, CTL exhibits a bimodal updraft profile for CCFAD broadening and for  $\overline{w(z)}$ , with a minimum near  $z = 7-8 \text{ km}$  (Figs. 9a-d). This structure has been documented for tropical convection in modeling studies (Fierro et al. 2009; Wang 2014) and observationally (Yuter and Houze 1995b; Hildebrand 1996; May and Rajopadhyaya 1996), with the upper-level peak attributed to ice LHR processes (Zipser 2003; Romps and Kuang 2010;

Fierro et al. 2012). The CTL rainband vertical motion profiles show little changes from the early RI period to the time of peak  $V_{MAX}$ , which should be expected given that TC intensification is controlled primarily by inner-core processes (Ooyama 1982). Five hours into RI (Figs. 9a,b), the NFUS updraft CCFAD and  $\overline{w(z)}$  profiles are nearly identical

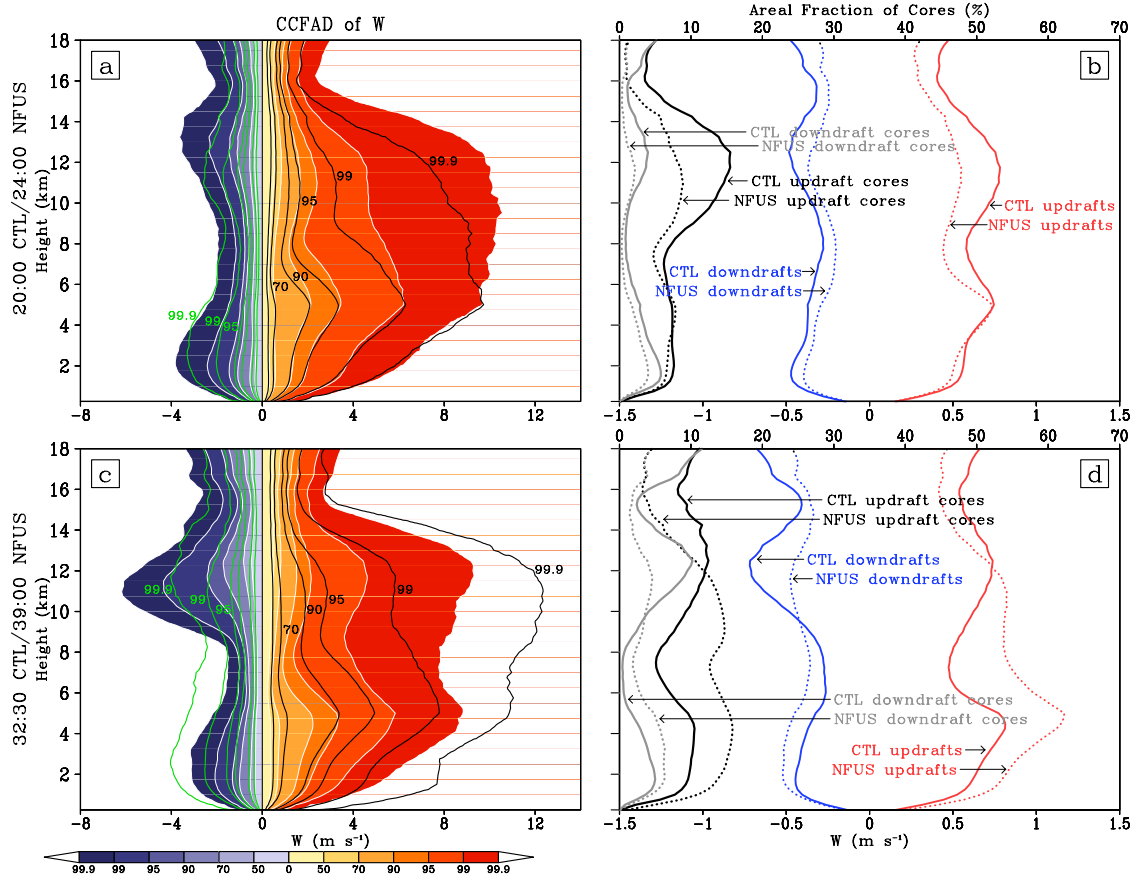


Figure 9. As in Fig. 8 but for the outer rainband region.

below  $z = 5$  km, roughly the freezing level, but above this altitude the NFUS updrafts become weaker, particularly for the strongest 1%. These results suggest that depositional LHR enhances the upper-level updraft peak associated with buoyant convective elements embedded in the outer rainbands. At the time of peak  $V_{MAX}$  (Figs. 9c,d), NFUS shows greater CCFAD broadening and a stronger  $\overline{w(z)}$  relative to CTL, but above  $z = 12$  km

these differences become greatly reduced, or reversed in sign for the case of  $\overline{w(z)}$ , implying that reduced depositional LHR still has an impact on NFUS updrafts at the upper levels. The larger updraft core fraction in NFUS below  $z = 12$  km suggests that the CCFAD and  $\overline{w(z)}$  profiles are reflecting a larger areal coverage of vigorous convection in the outer rainbands at this time (Figs. 3c,g).<sup>3</sup> Both CTL and NFUS exhibit a bimodal structure in the downdraft CCFADs, downdraft core fraction, and downdraft  $\overline{w(z)}$  profiles (Figs. 9a-d). Our results support the findings of Yuter and Houze (1995a,b), who reported upper-level downdraft peaks adjacent to upper-level updraft peaks in ordinary tropical convection. The CTL upper-level downdraft peak shows greater CCFAD broadening for both times (Figs. 9a,c), suggesting that updraft enhancement from depositional LHR (and also possibly, sublimative cooling from detrained hydrometeors) may play a key role in inducing upper-level compensating subsidence adjacent to convective elements in TC rainbands.

---

<sup>3</sup> Note for NFUS (Fig. 3g) the expansive band of high radar reflectivity with an embedded CB element cluster in the southern and eastern quadrants, much of which lies outside of 47-km radius, the inner cutoff radius used for rainbands at this time.

## Chapter 6. Thermodynamic Characteristics of Convective Bursts

In view of the important roles of CBs in the RI of Wilma, we examine the thermodynamic soundings of two selected CBs: one in CTL and the other in NFUS, observed in the developing eyewall 5 h into RI (20:00 CTL/24:00 NFUS). Figs. 10a,b compare the CB horizontal distribution in relation to upper-level vertical motion and column-integrated total frozen hydrometeors. Note the inward-directed subsidence bands flanking several of the strongest convective cores, peaking at  $7 \text{ m s}^{-1}$  in CTL and  $3 \text{ m s}^{-1}$  in NFUS (see arrows), that are similar to observations of Hurricane Bonnie (Heymsfield et al. 2001). Clearly, the CBs in NFUS can still induce subsidence directed into the eye, which is consistent with the fact that NFUS still undergoes RI. For CTL, CB elements and peak column-integrated frozen hydrometeors show a remarkably strong spatial correlation (see arrows). This correlation for NFUS is somewhat weaker, especially for the CB elements in the northern eyewall, which are located several kilometers radially inward from peak column frozen hydrometeors. While it might be tempting to conclude that these differences provide further evidence of depositional LHR enhancing CB updrafts, we must keep in mind that for NFUS, the increased eyewall tilt may account for the radial displacement. A three-dimensional analysis of CB updrafts in a future study might provide us with a better understanding of the relative impacts of surface heat fluxes and upper-level ice LHR processes in the generation of CBs.

Now we zoom in on two CBs, one from each simulation, contained within the 15 degree azimuthal slices marked by dashed lines in Figs. 10a,b. Their height-radial cross sections, given in Figs. 10c,d, show an outwardly titled updraft core peaking in the upper troposphere, an upper level outflow layer (centered 1 km lower for NFUS), and a deep

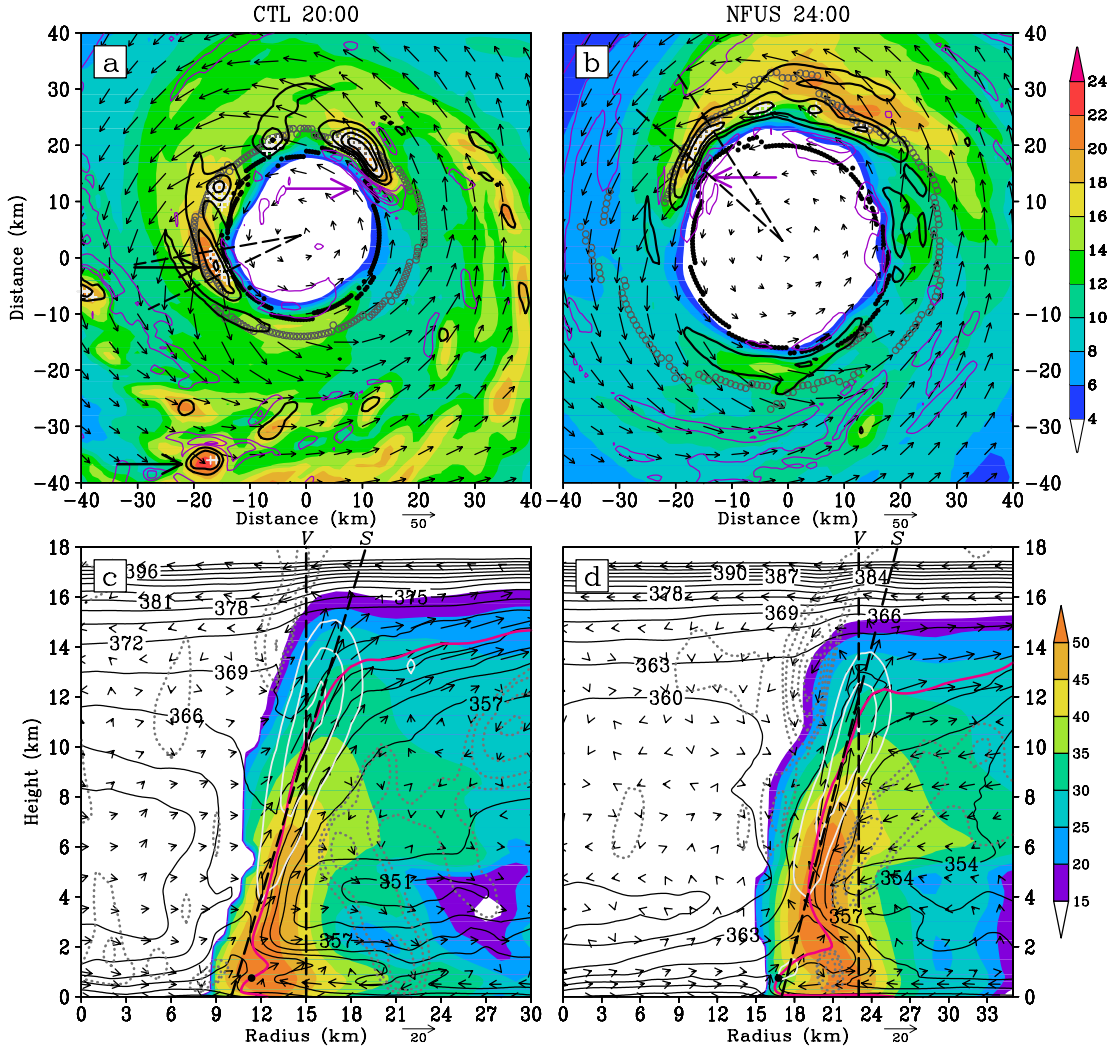


Figure 10. Total frozen hydrometeors integrated from 6-16 km (shaded,  $10^2 \text{ kg kg}^{-1}$ ) with horizontal storm-relative flow vectors ( $\text{m s}^{-1}$ ), vertical motion (upward, black contours, every  $5 \text{ m s}^{-1}$ ; downward, purple contours,  $-7, -5, -3, -1 \text{ m s}^{-1}$ ) and CB elements (white crosses) taken from (a) 20:00 CTL at  $z = 13 \text{ km}$ , and (b) 24:00 NFUS at  $z = 11 \text{ km}$ . Local  $z = 1\text{-km}$  and  $z = 11\text{-km}$  RMW are marked by black dots and gray circles, respectively. Dashed lines mark slice boundaries for azimuthal averaging in radial-height sections (c) and (d), which show radar reflectivity (shaded,  $\text{dBz}$ ),  $\theta_e$  (black contours,  $\text{K}$ ), vertical motion (upward, white contours, every  $5 \text{ m s}^{-1}$ ; downward, dotted gray contours,  $-4, -3, -2, -1, -0.5 \text{ m s}^{-1}$ ), and AAM (magenta contour,  $5 \times 10^5 \text{ s}^{-1}$ , 1.4 for CTL, 2.0 for NFUS), with in-plane flow vectors (vertical motions multiplied by 2). Slanted and vertical sounding lines are labeled with “S” and “V,” respectively. Black dots in (c) and (d) mark parcel lifting points used for SCAPE calculations.

layer descent of stratospheric origin flowing down the inner edge of the updraft core. CTL, unlike NFUS, shows a positive  $\theta_e$  anomaly occurring between the updraft inner edge and core above  $z = 11$  km (Fig. 10c). This  $\theta_e$  anomaly appears to result from the upward transport of higher  $\theta_e$  air from the lower layers and the downward transport of higher  $\theta_e$  air from the upper levels, given the near conservation of  $\theta_e$ . Similar features have been shown in CTL at RI onset (Fig. 6 in CZ13). Since water vapor mixing ratios are extremely small at this altitude,  $\theta_e$  should be nearly equivalent to  $\theta$ . The fact that relative humidity associated with the  $\theta_e$  anomaly region (not shown) is greater than 90% suggests that it is caused by excessive LHR in the eyewall updrafts that could not be compensated by adiabatic cooling.

Figure 11 compares slantwise environmental soundings in CTL (a,b) and NFUS (c,d). For both simulations, the slantwise sounding, taken through the tilted updraft cores to approximate the paths of rising parcels in the radial-height plane, closely follows lines of constant  $\theta_e$  (i.e., 366K for CTL and 364K for NFUS) and AAM in a deep layer. The skew  $T$ -log  $p$  plots show a saturated environment neutral to moist ascent from the MBL through 200 hPa in both CTL (Fig. 11a) and NFUS (Fig. 11c), which is consistent with the WISHE hypothesis (Emanuel 1986, Emanuel et al. 1994). Although these soundings are not representative of three-dimensional parcel trajectories, which have been shown to wrap azimuthally around the eyewall (Braun 2002), we demonstrate that a slantwise neutral sounding can also be used to characterize the thermodynamic conditions of a CB. Nevertheless, the fact that these soundings may not be entirely representative of the local environment surrounding rising parcels, particularly given the rapid decline of azimuthally-averaged environmental  $\theta_e$  with outward radial extent from the updraft core

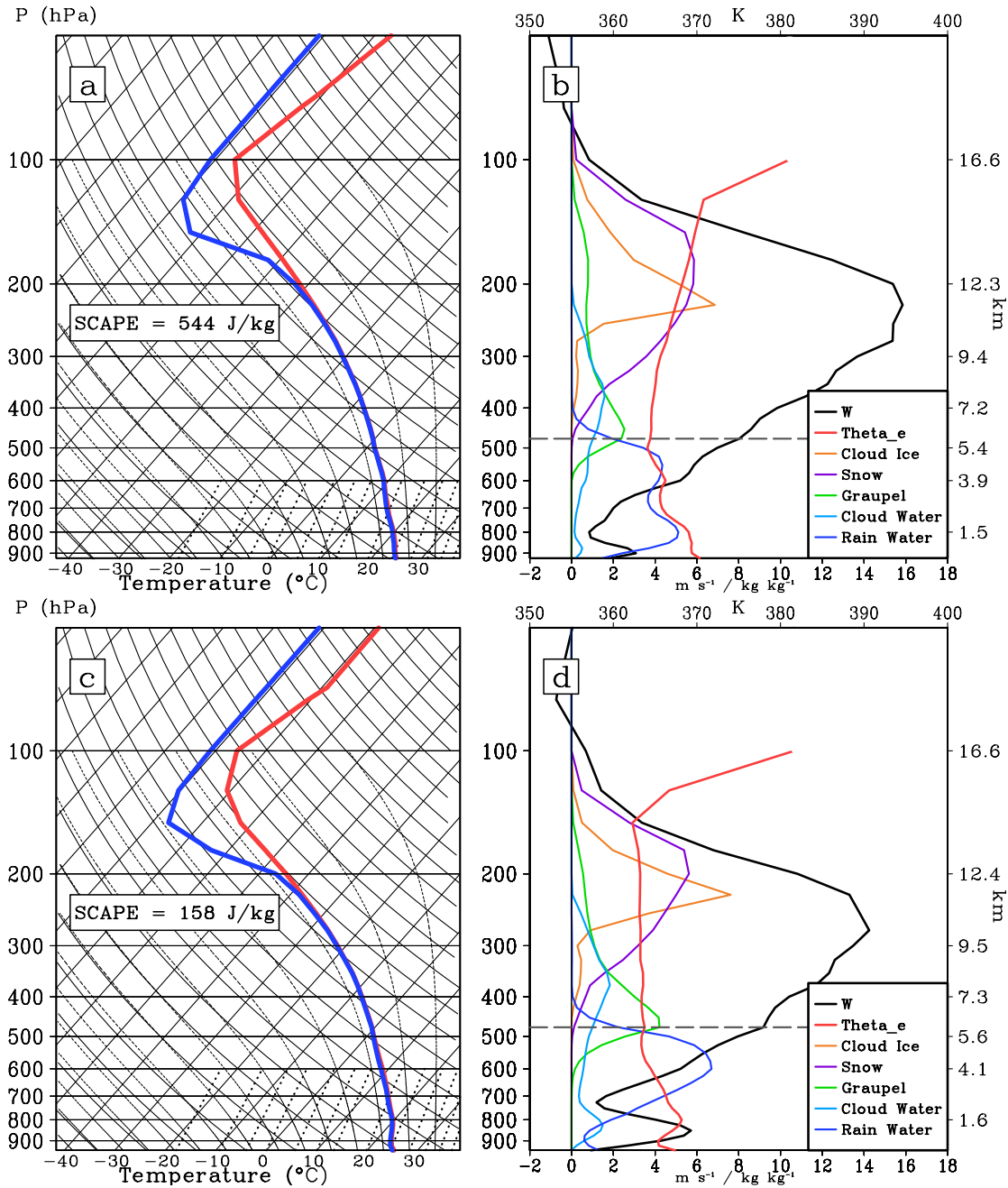


Figure 11. Left panels: skew  $T$ -log  $p$  diagrams for (a) CTL and (c) NFUS, with environmental variables taken from slanted sounding lines ( $S$ ), and with SCAPE computed along constant AAM lines, both from Fig. 10. Right panels: profiles along the slanted sounding lines of vertical motion ( $\text{m s}^{-1}$ ),  $\theta_e$  (K), and cloud species mixing ratios ( $\text{kg kg}^{-1}$ ;  $\times 10^5$ ) for cloud ice, ( $\times 10^3$ ) for snow, graupel, cloud water, and rain) for (b) CTL and (d) NFUS. Dotted gray line marks the approximate freezing level height. For (a)-(d) top of plot marks 50 hPa level.

(Figs. 10c,d), suggests that buoyant updrafts may still occur in an eyewall CB. Substantial evidence for eyewall buoyancy on the convective scale exists, possibly resulting from the temporary steepening of  $\theta_e$  with respect to AAM surfaces in their vertical tilt (Black et al. 1994), outward parcel displacement into a lower virtual temperature environment by low-level outflow (Braun 2002), or from the venting of high- $\theta_e$  air out of the eye region (Liu et al. 1999; Persing and Montgomery 2003; Eastin et al. 2005). Furthermore, an environment neutral to pseudoadiabatic moist ascent may still support parcel buoyancy when ice LHR processes are accounted for.

To investigate local buoyancy in these CBs, SCAPE is calculated along constant-AAM surfaces running through the center of the updraft cores that closely parallel the slanted sounding lines (Figs. 10c,d). The more than threefold increase of eyewall undilute SCAPE for CTL with ice LHR allowed over that of NFUS with ice LHR neglected (Figs. 11a,c) suggests that parcel warming from the latent heat of fusion (through both depositional and freezing processes) might be an important contributor to local buoyancy in the eyewall. While the neglect of freezing processes in the NFUS SCAPE calculation might render this value a bit conservative, it is still sufficient to generate  $w_{\max} > 17 \text{ m s}^{-1}$ .

Figs. 11b,d compare profiles of vertical motion, cloud species mixing ratios, and  $\theta_e$  between the two simulations. In general, the cloud species profiles are fairly similar, with cloud ice and snow peaking in the 150-300 hPa layer, and graupel, formed by the riming of ice and snow, peaking just above the freezing level where supercooled water is more abundant. The vertical motion profiles show a similar shape with peak magnitudes of  $16 \text{ m s}^{-1}$  for CTL and  $14 \text{ m s}^{-1}$  for NFUS, but note that the CTL updraft peaks 1.5 km

higher, closer to the maximum snow and ice mixing ratios. Possible entrainment effects and negative perturbation pressure gradient forces, both neglected in our analysis, might account for the peak CTL and NFUS updraft magnitudes falling short of the  $w_{\max}$  predicted by SCAPE. Also noteworthy is the nearly constant  $\theta_e$  profile in NFUS over the 550-150 hPa layer, which contrasts from the CTL profile showing a gradual  $\theta_e$  increase above a midlevel minimum. Fierro et al. (2009, 2012) showed  $\theta_e$  traces with shapes similar to the CTL profile for parcels rising through tropical oceanic cumulonimbus, and they attributed the midlevel minimum to dilution and the recovery at higher levels to LHR from ice processes. Since  $\theta_e$  is conserved with respect to the latent heat of vaporization, the absence of a  $\theta_e$  increase at higher levels in NFUS is consistent with the removal of the fusion component of  $L_d$ .

To illustrate how slantwise, as opposed to vertical, soundings through the eyewall provide a more realistic representation of the thermodynamic environment, Fig. 12 shows soundings taken along vertical lines marked “V” in Figs. 10c,d, which extend downward from the upper portions of the updraft cores. The near dry adiabatic but saturated layer in the 750-800 hPa layer in Fig. 12a would imply an absolute unstable condition for upright motion, but here it just reflects an upward transition from the MBL with a  $\theta_e$  minimum near  $z = 4$  km characterized by subsaturated conditions (cf. Figs. 10c and 12a,b). Above the  $\theta_e$  minimum, the sounding penetrates into the higher- $\theta_e$  updraft core, with a stable lapse rate between 400 and 250 hPa. The NFUS vertical soundings (Figs. 12c,d) show similar trends, with an increase in  $\theta_e$  now evident with upward extent from the unsaturated midlevel downdraft region into the saturated updraft core. Note that unlike in

CTL,  $\theta_e$  no longer increases above  $z = 11$  km, where cloud ice and snow peak and where depositional growth should be maximized.

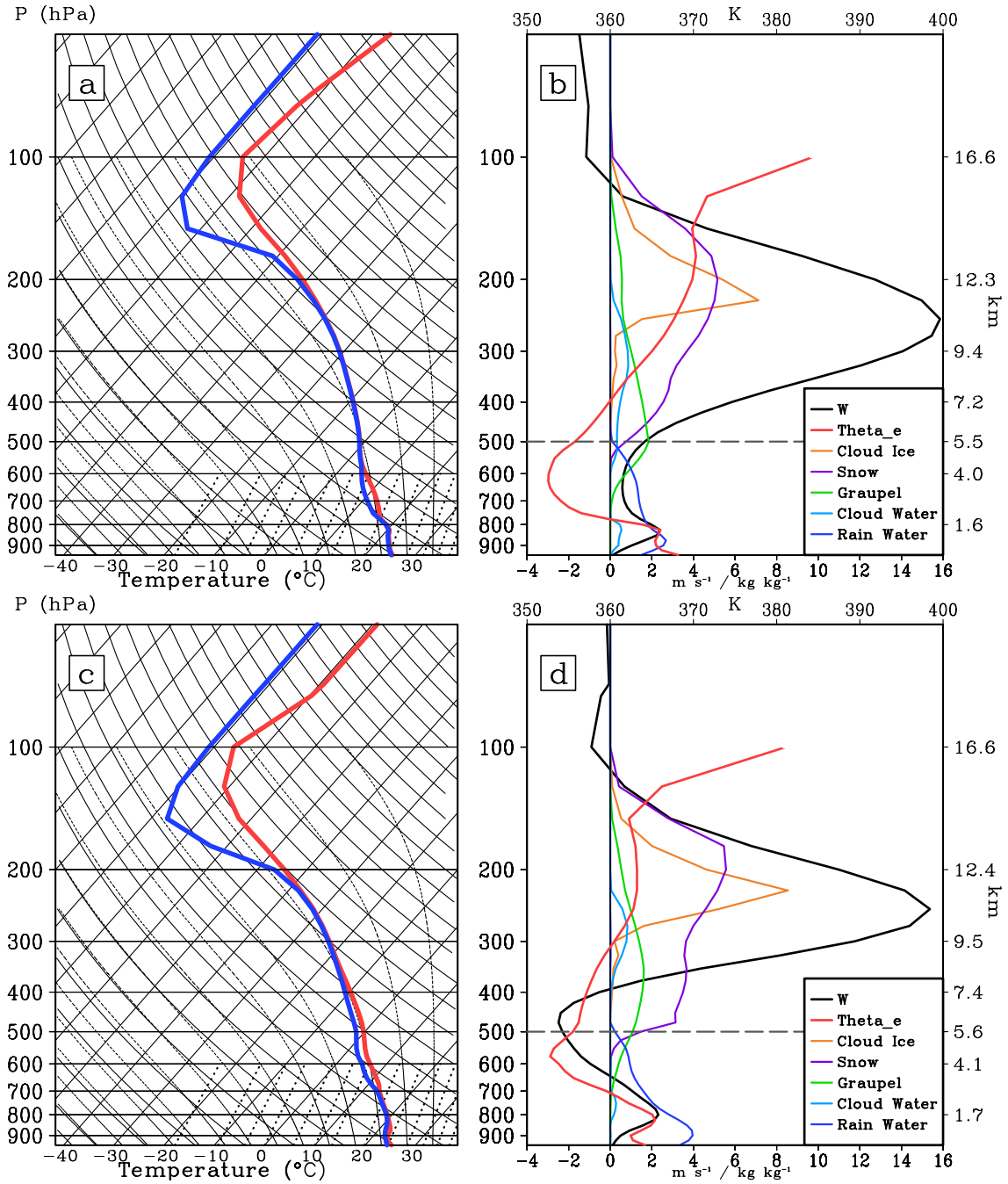


Figure 12. As in Fig. 11 but for vertical sounding lines (V) from Fig. 10.

## Chapter 7. Summary and Conclusions

In this study, the impacts of the latent heat of fusion on the RI of Hurricane Wilma (2005) are examined by comparing a 72-h control simulation of the storm to a sensitivity simulation in which the latent heat of deposition is reduced by removing the fusion component. Although the NFUS storm still undergoes RI, the RI onset is delayed by 4 hours, the duration is 5 hours shorter, and the average deepening rate is reduced (3.0 hPa h<sup>-1</sup> versus 3.7 hPa h<sup>-1</sup> in CTL). For both storms, the RI period is characterized by lowering upper-level isentropic surfaces and the development of anomalous warming near  $z = 14$  km in the eye. At the time of peak intensity, the NFUS storm is 30 hPa weaker in  $P_{\text{MIN}}$ , with upper level warming reduced by 8°C.

During the pre-RI and RI periods, NFUS shows, on average, a lower number of CB elements inside the  $z = 11$ -km RMW. These results are supported by CCFAD diagrams composited from a 2-h period early in the RI phase which feature stronger eyewall updrafts in CTL, most notably in the upper troposphere for the highest percentiles of the velocity range. The eyewall CCFADs also show stronger subsidence above  $z = 14$  km in CTL. At the time of peak  $V_{\text{MAX}}$ , CTL displays a stronger azimuthally-averaged secondary circulation. For both simulations, the outer rainbands are characterized by weaker vertical motion relative to the eyewall, although depositional heating appears to enhance updrafts and the associated compensating subsidence at the upper levels as well.

Soundings taken through the updraft cores of selected CBs inside the upper-level RMW during RI reveal neutral to slantwise moist ascent. The altitude of peak vertical motion in CTL is 1.5 km higher than in NFUS, closer to the highest cloud ice and snow

mixing ratios. For CTL  $\theta_e$ , which is conserved with respect to condensation but not fusion, shows a gradual increase with height from the freezing level to the tropopause, but for NFUS it remains nearly constant over this altitude range, which should be expected, given the removal of the fusion contribution to  $L_d$ . Furthermore, SCAPE calculations reveal ice LHR processes to be an important factor in generating sufficient conditional instability to support CB updrafts in the eyewall.

The above results support our hypothesis that the ice LHR in the eyewall from depositional processes facilitates TC intensification through the generation of CBs. The extreme altitude reached by CB updrafts allows for the downward displacement of stratospheric air in compensating subsidence currents. RI commences once an upper-level cyclonic circulation can develop, which acts to protect warming over the eye from ventilation by environmental flows. The CB-induced subsidence warming then begins to concentrate to form an upper-level warm core, which hydrostatically enhances surface pressure falls. Enhanced radial pressure gradients in the lower levels spin up the tangential wind circulation from below. Despite the reduced impacts of depositional heating, the NFUS simulation nevertheless generates an intense 920-hPa TC that undergoes RI per the conventional definition, and we see evidence of upper-level subsidence directed toward the eye coincident with the development of a warm core. The fact that the NFUS storm remains in the same high-SST environment as CTL may account for the substantial, albeit reduced, number of inner-core CB elements that it generates prior to and during RI, and future work is needed for better understanding the relative impacts of surface heat fluxes and ice LHR processes on the generation of CBs.

This study nonetheless highlights the important contribution of the latent heat of fusion to TC RI through deposition in the eyewall, given favorable environmental conditions.

## Appendix I: Calculation of SCAPE

SCAPE is calculated from azimuthally-averaged variables following Craig and Gray (1996) using the integral

$$\text{SCAPE} = g \int_{LCL}^{LNB} \left[ \frac{T_{vp} - T_{ve}}{T_{ve}} \right]_{AAM} dz \quad (1)$$

where  $T_{vp}$  and  $T_{ve}$  denote parcel and environmental virtual temperatures, respectively, and  $g$  is the gravitational constant. Although the limits of integration run from the lifting condensation level (LCL) to the level of neutral buoyancy (LNB), negative areas between these limits (also referred to as convective inhibition) are not included in the summation. SCAPE is equivalent to CAPE, except for the fact that the vertical coordinate  $z$  follows surfaces of constant absolute angular momentum (AAM), given by

$$\text{AAM} = r(V + fr/2) \quad (2)$$

where  $r$  is the radius,  $V$  is the tangential wind, and  $f$  is the Coriolis parameter. The SCAPE integration is terminated for AAM surfaces extending more than 30 km beyond the lifted parcel radius prior to the LNB being reached. Enforcing this limit ensures that for parcels lifted from the eyewall (the region of focus for our study), the SCAPE integration does not extend radially beyond a path physically consistent with the modeled slantwise convection, given the tendency for AAM surfaces to become nearly horizontal in the upper troposphere. A parcel lifting height of  $z = 0.75$  km, chosen for its close proximity to the top of the MBL, is used for both CTL and NFUS. Parcel AAM is kept constant above this height by interpolating through the radial-height grid.

Lifted parcel temperatures for both CTL and NFUS are calculated using reversible thermodynamics (all condensate retained in rising parcels). While the effects of

entrainment are not considered here, they should be less significant for the inner-core region given the high ambient mid-tropospheric relative humidity (Molinari et al. 2012); furthermore, any overestimate of SCAPE based on neglecting entrainment should be partially compensated by (or perhaps overcompensated by) our neglecting hydrometeor fallouts from rising parcels. Since following a reversible adiabat requires the tracking of hydrometeor mixing ratios, we utilize a simplified 3-species (vapor, liquid, and ice) microphysics parameterization outlined in Bryan and Fritsch (2004). Thus, while the initial parcel properties are obtained from the WRF model output, the computation of parcel temperatures along AAM surfaces uses a simplified alternative to the Thompson microphysics. Details of this 3-species scheme can be found in Bryan and Fritsch (2004); in summary, it assumes vapor saturation with respect to water between the LCL and the freezing level, saturation with respect to ice for temperatures below  $-40$  °C, and for the layer in between, the calculation of supercooled liquid and ice mixing ratios uses a linear weighting technique.

Lifted parcel temperatures are computed using

$$\frac{D \ln \theta}{Dt} = \left[ \frac{R_m}{c_{pml}} - \frac{R}{c_p} \right] \frac{D \ln p}{Dt} + \frac{L_v}{c_{pml} T} \frac{Dr_l}{Dt} + \frac{L_d}{c_{pml} T} \frac{Dr_i}{Dt} \quad (3)$$

following Equations 4 and 8 in Bryan and Fritsch (2004), with mixing ratio  $r$  designated by the subscript  $l$  or  $i$  for liquid or ice, respectively,  $R_m$  and  $R$  as the gas constants for moist and dry air,  $c_{pml}$  as the total specific heat at constant pressure (weighted by liquid, vapor, and ice mixing ratios), and with  $c_p$  as the specific heat of dry air at constant pressure. For CTL, ice production above the freezing level allows for parcel warming by the latent heat of fusion ( $L_f = L_d - L_v$ ) both for freezing ( $dr_i = -dr_l$ ) and for deposition ( $dr_i$

$> 0$ ,  $dr_i = 0$ ).<sup>4</sup> However, for NFUS, ice production is not permitted, forcing the accumulation of supercooled condensate above the freezing level, thus not allowing  $L_f$  to warm the parcel by either freezing or deposition processes.

---

<sup>4</sup> Using reversible thermodynamics with ice processes included is considered the most accurate method for calculating undilute CAPE in the tropical environment within the constraints of parcel theory (Williams and Renno 1993), although calculations with partial hydrometeor fallout have been performed on occasion (Romps and Kuang 2010).

## References

- Black, M. L., R. W. Burpee, and F. D. Marks, Jr., 1996: Vertical motion characteristics of tropical cyclones determined with airborne Doppler radial velocities. *J. Atmos. Sci.*, **53**, 1887-1909.
- Black, R. A., H. B. Bluestein, and M. L. Black, 1994: Unusually strong vertical motions in a Caribbean hurricane. *Mon. Wea. Rev.*, **122**, 2722-2739.
- Bolton, D., 1980: The computation of equivalent potential temperature. *Mon. Wea. Rev.*, **108**, 1046-1053.
- Braun, S. A., 2002: A cloud-resolving simulation of Hurricane Bob (1991): Storm structure and eyewall buoyancy. *Mon. Wea. Rev.*, **130**, 1573-1592.
- Bryan, G. H., and J. M. Fritsch, 2004: A reevaluation of ice-liquid water potential temperature. *J. Atmos. Sci.*, **132**, 2421-2431.
- Chen, H., D.-L. Zhang, J. Carton, and R. Atlas, 2011: On the rapid intensification of Hurricane Wilma (2005). Part I: Model prediction and structural changes. *Wea. Forecasting*, **26**, 885-901.
- , and D.-L. Zhang, 2013: On the Rapid Intensification of Hurricane Wilma (2005). Part II: Convective bursts and the upper-level warm core. *J. Atmos. Sci.*, **70**, 146-162.
- Craig, G. C., and S. L. Gray, 1996: CISK or WISHE as the mechanism for tropical cyclone intensification. *J. Atmos. Sci.*, **53**, 3528-3540.
- Eastin, M. D., W. M. Gray, and P. G. Black, 2005: Buoyancy of convective vertical motions in the inner core of intense hurricanes. Part II: Case studies. *Mon. Wea. Rev.*, **133**, 209-227.

- Emanuel, K. A., 1986: An air-sea interaction theory for tropical cyclones. Part I: Steady-state maintenance. *J. Atmos. Sci.*, **43**, 585-604.
- , J. D. Neelin, and C. S. Bretherton, 1994: On large-scale circulations in convecting atmospheres. *Quart. J. Roy. Meteor. Soc.*, **120**, 1111-1143.
- Fierro, A. O., J. Simpson, M. A. LeMone, J. M. Straka, and B. F. Smull, 2009: On how hot towers fuel the Hadley Cell: An observational and modeling study of line-organized convection in the Equatorial Trough from TOGA COARE. *J. Atmos. Sci.*, **66**, 2730-2746.
- , and J. M. Reisner, 2011: High-resolution simulation of the electrification and lightning of Hurricane Rita during the period of rapid intensification. *J. Atmos. Sci.*, **68**, 477-494.
- , E. J. Zipser, M. A. LeMone, J. M. Straka, and J. Simpson, 2012: Tropical oceanic hot towers: Need they be undilute to transport energy from the boundary layer to the upper troposphere effectively? An answer based on trajectory analysis of a simulation of a TOGA COARE convective system. *J. Atmos. Sci.*, **69**, 195-213.
- Foley, G., 1998: A marked upper tropospheric temperature anomaly observed by an aircraft near a thunderstorm over inland Western Australia. *Aust. Meteor. Mag.*, **47**, 321-326
- Franklin, J. L., R. J. Pasch, L. A. Avila, J. L. Beven II, M. B. Lawrence, S. R. Stewart, and E. S. Blake, 2006: Atlantic Hurricane Season of 2004. *Mon. Wea. Rev.*, **134**, 981-1025.
- Frisius, T., and D. Schönemann, 2012: An extended model for the potential intensity of tropical cyclones. *J. Atmos. Sci.*, **69**, 641-661.

- Guimond, S. R., G. M. Heymsfield, and F. J. Turk, 2010: Multiscale observations of Hurricane Dennis (2005): The effects of hot towers on rapid intensification. *J. Atmos. Sci.*, **67**, 633-654.
- Hack, J. J., and W. H. Schubert, 1986: Nonlinear response of atmospheric vortices to heating by organized cumulus convection. *J. Atmos. Sci.*, **43**, 1559-1573.
- Heymsfield, G. M., J. B. Halverson, J. Simpson, L. Tian, and T. P. Bui, 2001: ER-2 Doppler radar investigations of the eyewall of Hurricane Bonnie during the Convection and Moisture Experiment-3. *J. Appl. Meteor.*, **40**, 1310-1330.
- Hildebrand, P. H., and Coauthors, 1996: The ELDORA/ASTRAIA airborne Doppler weather radar: High-resolution observations from TOGA COARE. *Bull. Amer. Meteor. Soc.*, **77**, 213-232.
- Holland, G. J., T. D. Keenan, and G. D. Crane, 1984: Observations of a phenomenal temperature perturbation in Tropical Cyclone Kerry (1979). *Mon. Wea. Rev.*, **112**, 1074-1082.
- Holliday, C. R., and A. H. Thompson, 1979: Climatological characteristics of rapidly intensifying typhoons. *Mon. Wea. Rev.*, **107**, 1022-1034.
- Houze, R. A., Jr., 2010: Clouds in tropical cyclones. *Mon. Wea. Rev.*, **138**, 293-344.
- Jorgensen, D. P., E. J. Zipser, and M. A. LeMone, 1985: Vertical motions in intense hurricanes. *J. Atmos. Sci.*, **42**, 839-856.
- Kaplan, J., and M. DeMaria, 2003: Large-scale characteristics of rapidly intensifying tropical cyclones in the North Atlantic basin. *Wea. Forecasting*, **18**, 1093-1108.
- Kieu, C. Q., H. Chen, and D.-L. Zhang, 2010: An examination of the pressure-wind relationship for intense tropical cyclones. *Wea. Forecasting*, **25**, 895-907.

- Lawrence, M. B., B. M. Mayfield, L. A. Avila, R. J. Pasch, and E. N. Rappaport, 1998: Atlantic hurricane season of 1995. *Mon. Wea. Rev.*, **126**, 1124-1151.
- , L. A. Avila, J. L. Beven, J. L. Franklin, J. L. Guiney, and R. J. Pasch, 2001: Atlantic hurricane season of 1999. *Mon. Wea. Rev.*, **129**, 3057-3084.
- Liu, Y., D.-L. Zhang, and M. K. Yau, 1999: A multiscale numerical study of Hurricane Andrew (1992). Part II: Kinematics and inner-core structures. *Mon. Wea. Rev.*, **127**, 2597-2616.
- Marks, F. D., Jr., and R. A. Houze, Jr., 1987: Inner core structure of Hurricane Alicia from airborne Doppler radar observations. *J. Atmos. Sci.*, **44**, 1296-1317.
- May, P. T., and D. K. Rajopadhyaya, 1996: Wind profiler observations of vertical motion and precipitation microphysics of a tropical squall line. *Mon. Wea. Rev.*, **124**, 621-633.
- Molinari, J., P. Moore, and V. Idone, 1999: Convective structure of hurricanes as revealed by lightning locations. *Mon. Wea. Rev.*, **127**, 520–534.
- , and D. Vollaro, 2010: Rapid intensification of a sheared tropical storm. *Mon. Wea. Rev.*, **138**, 3869-3885.
- , D. M. Romps, D. Vollaro, and L. Nguyen, 2012: CAPE in tropical cyclones. *J. Atmos. Sci.*, **69**, 2452-2463.
- Ooyama, K. V., 1982: Conceptual evolution of the theory and modeling of the tropical cyclone. *J. Meteor. Soc. Japan*, **60**, 369-380.
- Persing, J., and M. T. Montgomery, 2003: Hurricane superintensity. *J. Atmos. Sci.*, **60**, 2349-2371.

- Price, C., M. Asfur, and Y. Yair, 2009: Maximum hurricane intensity preceded by increase in lightning frequency. *Nat. Geosci.*, **2**, 329-332.
- Rodgers, E. B., W. S. Olson, V. M. Karyampudi, and H. F. Pierce, 1998: Satellite-derived latent heating distribution and environmental influences in Hurricane Opal (1995). *Mon. Wea. Rev.*, **126**, 1229-1247.
- , —, J. Halverson, J. Simpson, and H. Pierce, 2000: Environmental forcing of Supertyphoon Paka's (1997) latent heat structure. *J. Appl. Meteor.*, **39**, 1983-2006.
- Rogers, R., S. Aberson, J. Kaplan, and S. Goldenberg, 2002: A pronounced upper-tropospheric warm anomaly encountered by the NOAA G-IV aircraft in the vicinity of deep convection. *Mon. Wea. Rev.*, **130**, 180-187.
- Rogers, R. R. and M. K. Yau, 1989: *A Short Course in Cloud Physics*, 3rd ed. Elsevier, 290 pp.
- Romps, D. M., and Z. Kuang, 2010: Do undiluted convective plumes exist in the upper tropical troposphere? *J. Atmos. Sci.*, **67**, 468-484.
- Rotunno, R., and K. A. Emanuel, 1987: An air-sea interaction theory for tropical cyclones. Part II: Evolutionary study using a nonhydrostatic axisymmetric numerical model. *J. Atmos. Sci.*, **44**, 542-561.
- Thompson, G., R. M. Rasmussen, and K. Manning, 2004: Explicit forecasts of winter precipitation using an improved bulk microphysics scheme. Part I: Description and sensitivity analysis. *Mon. Wea. Rev.*, **132**, 519-542.
- , P. R. Field, R. M. Rasmussen, and W. D. Hall, 2008: Explicit forecasts of winter precipitation using an improved bulk microphysics scheme. Part II: Implementation of a new snow parameterization. *Mon. Wea. Rev.*, **136**, 5095-5115.

- Velden, C. S., and W. L. Smith, 1983: Monitoring tropical cyclone evolution with NOAA satellite microwave observations. *J. Climate Appl. Meteor.*, **22**, 714-724.
- Wang, H., and Y. Wang, 2014: A numerical study of Typhoon Megi (2010). Part I: Rapid intensification. *Mon. Wea. Rev.*, **142**, 29-48.
- Wang, Z., 2014: Characteristics of convective processes and vertical velocity from the tropical wave to tropical cyclone stage in a high-resolution numerical model simulation of Tropical Cyclone Fay (2008). *J. Atmos. Sci.*, **71**, 896-915.
- Williams, E. and N. Renno, 1993: An analysis of the conditional instability of the tropical atmosphere. *Mon. Wea. Rev.*, **121**, 21-36.
- Yuter, S. E., and R. A. Houze, Jr., 1995: Three-dimensional kinematic and microphysical evolution of Florida cumulonimbus. Part I: Spatial distribution of updrafts, downdrafts, and precipitation. *Mon. Wea. Rev.*, **123**, 1921-1940.
- , and —, 1995: Three-dimensional kinematic and microphysical evolution of Florida cumulonimbus. Part II: Frequency distributions of vertical velocity, reflectivity, and differential reflectivity. *Mon. Wea. Rev.*, **123**, 1941–1963.
- Zhang, D.-L., Y. Liu, and M. K. Yau, 2001. A multiscale numerical study of Hurricane Andrew (1992): Part IV: Unbalanced flows. *Mon. Wea. Rev.*, **129**, 92-107.
- , and C. Q. Kieu, 2006: Potential vorticity diagnosis of a simulated hurricane. Part II: Quasi-balanced contributions to forced secondary circulations. *J. Atmos. Sci.*, **63**, 2898-2914.
- , and H. Chen, 2012: Importance of the upper-level warm core in the rapid intensification of a tropical cyclone. *Geophys. Res. Lett.*, **39**, L02806, doi:10.1029/2011GL050578.

Zipser, E. J., 2003: Some views on “hot towers” after 50 years of tropical field programs and two years of TRMM data. *Cloud Systems, Hurricanes, and the Tropical Rainfall Measuring Mission (TRMM)*, *Meteor. Monogr.*, **29**, 49-58